

Achieving a Columnar-to-Equiaxed Transition Through Dendrite Twinning in High Deposition Rate Additively Manufactured Titanium Alloys



A.E. DAVIS, J. WAINWRIGHT, V.K. SAHU, D. DREELAN, X. CHEN, J. DING, T. FLINT, S. WILLIAMS, and P.B. PRANGNELL

The coarse β -grain structures typically found in titanium alloys like Ti-6Al-4V (wt pct, Ti64) and Ti-6Al-2Sn-4Zr-2Mo-0.1Si (Ti6242), produced by high deposition rate additive manufacturing (AM) processes, are detrimental to mechanical performance. Certain modified processing conditions have been shown to lead to a more refined grain structure, which has generally been attributed to a change in the solidification conditions with respect to the experimental Hunt diagram proposed by Semiatin and Kobryn. It is shown that with Wire Arc AM (WAAM) increasing the wire feed speed (WFS) is effective in promoting a columnar-to-equiaxed transition (CET). Conversely, estimates of the dendrite-tip undercooling using the KGT model suggest that this will be too small for free nucleation without the addition of artificial nucleants, due to the very low solute partitioning in Ti alloys. It is also shown that it is difficult to promote a CET with plasma transferred arc WAAM as computational fluid dynamics (CFD) melt-pool simulations indicate that the solidification parameters remain within the columnar region on the Semiatin-Kobryn Hunt map, within the constraints of a stable process. However, a high fraction of twin boundaries was observed in the refined β -grain structures seen at high WFS. This has been attributed to departure of $\langle 001 \rangle_{\beta}$ alignment from the direction of maximum thermal gradient, caused by the curvature of the fusion boundary, stimulating dendrite twinning during solidification. In addition, it is shown that increasing the WFS leads to a change in melt-pool geometry and a reduction of remelt depth, which promoted dendrite twinning and grain refinement.

<https://doi.org/10.1007/s11661-024-07388-7>
© The Author(s) 2024

I. INTRODUCTION

WIRE Arc Additive Manufacturing (WAAM) is a wire-fed, plasma-arc heat source, directed energy deposition (DED) process, capable of kilogram-per-hour deposition rates.^[1,2] Because of the high cost of producing and machining forgings, WAAM is particularly well suited to the production of large-scale titanium airframe components, owing to its high build rate, low capital equipment cost, short lead times, and unrestricted build

envelope.^[1,2] WAAM processes typically have melt-pool sizes of 5–10 mm in diameter and deposit layer heights of 1–2 mm.^[3–5] Despite the larger melt pool, compared to powder-bed AM, each deposition track still solidifies at cooling rates of < 100 °C/s,^[3,4,6] which is 1–2 orders of magnitude greater than that found in conventional Ti castings.

It has been widely reported that Ti alloys like Ti64 built with the WAAM process commonly exhibit very coarse columnar β -grain structures,^[7–11] which can have a negative effect on their mechanical properties.^[8,10–14] Although, on cooling to room temperature, Ti64 transforms from the primary β -grain structure to > 90 pct lamellar α .^[4,15–18] and the α variants that form inherit a texture from their coarse parent β grains due to the Burgers Orientation Relationship (BOR).^[19] When combined with the plastic heterogeneity promoted by the formation of grain boundary α allotriomorphs and single variant α colonies, which grow in from the β -grain boundaries, this can cause significant anisotropy and scatter in critical mechanical properties, such as ductility and fatigue crack growth rates.^[8,10–14,20]

A.E. DAVIS, V.K. SAHU, D. DREELAN, T. FLINT and P.B. PRANGNELL are with the Department of Materials, The University of Manchester, Manchester, M13 9PL, UK. Contact e-mail: alec.davis@manchester.ac.uk J. WAINWRIGHT, X. CHEN and S. WILLIAMS are with the Welding Engineering and Laser Processing Centre, Cranfield University, Bedfordshire, MK43 0PL, UK. J. DING is with the Welding Engineering and Laser Processing Centre, Cranfield University and also with the WAAM3D, Milton Keynes, MK14 6FD, UK.

Manuscript submitted November 17, 2023; accepted March 10, 2024.

The formation of coarse columnar grain structures in Ti64 AM deposits is related to the metallurgy of the Ti–Al–V system and the solidification conditions in a moving melt pool, combined with the incremental nature of AM processes. In Ti64, the main alloying elements Al and V have partition coefficients very close to 1, of $k_{Al} \sim 1.15$ and $k_V \sim 0.97$, respectively (although this can vary slightly with composition within the allowable range).^[4] Only Fe, the main trace element that is present at a low concentration (typically ~ 0.17 wt pct), has a lower value of $k_{Fe} = 0.38$.^[21,22] Electron probe micro-analysis (EPMA) evidence has confirmed these partition coefficients are consistent with the low levels of micro-segregation observed in Ti64 WAAM deposits, which lead to less than < 7 pct enrichment at the dendrite boundaries.^[4] This low level of solute partitioning limits the potential for constitutional undercooling at the solidification front.^[23]

Microstructure transitions in solidification can be correlated to the ratio of the thermal gradient in the liquid (G_L) at the solidification front relative to the solidification front velocity (v) which is related to the solutal undercooling.^[23,24] In terms of achieving an undercooling at the solidification front in an AM process, this weak solute partitioning is exacerbated by the positive thermal gradient always present in the liquid when a heated melt pool moves forward over colder previously solidified material.^[24] With a moving melt pool, the solidification front velocity is directly correlated to the energy source translation rate, and lower values of G_L/v can thus be achieved by increasing the process speed. This ratio will also be lowest at the top rear of the melt pool near the centerline^[25]; but in AM, this region is generally remelted when the next track is deposited. In addition, no artificial inoculants are currently used in commercial Ti alloys, resulting in a lack of efficient nucleants being available in a sufficient density to stimulate a columnar to equiaxed transition (CET) at low melt undercoolings.^[9,23] For example, when using the Hunt model^[26] with aluminum alloys that contain grain refiners, a nucleation density of $> 4 \times 10^5 \text{ mm}^{-3}$ and a critical undercooling of $< 1 \text{ K}$ are typically required to obtain an equiaxed grain structure under similar conditions during gas tungsten arc welding.^[27,28]

In high deposition rate AM with alloys like Ti64, after each melt track solidifies the material cools and transforms to α , with < 10 wt pct residual β ,^[29] as the cooling rates are not fast enough to produce martensite.^[19] However, as the heat source approaches to deposit the next track before remelting, the material reheats above the β transus causing the retained β to regrow and reform the primary β grain structure that developed in the previous pass.^[4,15,30] Reheating can also potentially lead to some solid-state grain coarsening.^[31,32] These reformed β grains are then partially remelted and become the new fusion boundary.^[4,30] The low level of solute partitioning and a lack of efficient nucleants in titanium alloys thus normally lead to solidification by the reformed β grains growing epitaxially from the fusion boundary, with little to no nucleation ahead of the solidification front. When this process is repeated

through multiple added layers, columnar growth is uninterrupted over large build heights, which selects favorably orientated grains with a common preferred $\langle 001 \rangle_\beta$ growth direction, leading to a strong texture and a very coarse, columnar grain structure.^[7,32,33]

Various methods have been investigated for promoting a more isotropic primary β grain structure in Ti64 AM, including inter-pass deformation by rolling and peening,^[8,11,30,33] adding artificial inoculants and growth restricting alloy additions,^[9,34–37] and ultrasonic vibration of the melt pool.^[38] However, these approaches tend to increase costs or have other disadvantages. For example, inoculation introduces brittle second-phase particles that are detrimental to the mechanical properties of Ti alloys^[37] and it is difficult to apply ultrasonic vibration to full-scale components. Perhaps more promisingly, it has been known for some time that modifying the process window to change the solidification conditions can promote more-equiaxed grain structures in Ti64 deposits built with DED processes.^[7,39] This has included increasing the wire feed speed,^[7,39] or adding a cold wire,^[40] as well as modifying the build strategy.^[39,41–45] Researchers reporting these techniques have often explained their success by the effect they are theoretically expected to have on the G_L/v ratio relative to the CET boundary on the experimental Hunt solidification diagram proposed by Kobryn and Semiatin^[46]; *i.e.*, by reducing G_L and/or increasing v , solidification will shift to the equiaxed region. However, when using a conventional arc energy source, the more extreme modified processing conditions required frequently lead to unsatisfactory control of the deposited bead geometry. Nevertheless, with the recent development of purpose-designed WAAM processes, it is worth exploring the underlying mechanisms that give rise to grain refinement by process control in more detail. For example, multi-energy source (MES) configurations that can combine the advantages of arc and laser processes to dynamically alter the layer geometry, while depositing at higher build rates through control of the energy profile, are currently being investigated.^[47]

Given the very low solute partitioning seen in alloys like Ti64, the apparent ability to cross the CET by this approach seems surprising. Firstly, while the results of Kobryn and Semiatin^[46] are clear, the Hunt model^[26] was fitted to their data (which we have reproduced below), with an apparent critical undercooling of 1.1 K and a nucleation site density of $5 \times 10^{14} \text{ m}^{-3}$, which implies a high nucleation efficiency. Secondly, the thermal gradient and solidification front velocity must be changed substantially to have a major impact as the material response, in terms of the dendrite-tip undercooling, is relatively insensitive in the solidification rate range accessible by WAAM processes. For example, in the solidification velocity range of $0.1\text{--}10 \text{ mm/s}$, the thermal gradient has only a small effect on the tip undercooling, and decreasing G_L will thus mainly only widen the mushy zone.^[47] The rate the Gibbs-Thompson dendrite-tip radius and solute-related undercoolings increase with growth velocity (as will be discussed below, explored through the classical Kurz, Giovanola

and Trivedi (KGT) model^[47]) are also low in this velocity range and the overall tip undercooling increases by a factor of less than 1.5. In addition, it is generally recognized that the thermal Peclet numbers are at least two orders of magnitude lower than solute Peclet numbers in metals, and the thermal undercooling will be negligible in a WAAM process.^[27]

From a process design point of view, it is therefore important to improve current understanding of the metallurgical principles that control the solidification conditions that lead to a breakdown of epitaxial-columnar β -grain growth in Ti alloys during AM. In this paper, we will hence first present new systematic results confirming that the CET can indeed apparently be crossed with the WAAM process, by varying the wire feed speed with two Ti alloys with a similar α/β phase balance—Ti64 and Ti6242 (building upon preliminary results of a previous study).^[48,49] Results from a CFD model of the deposition process, which takes into account melt-pool convection, will then be used to estimate values of G_L and v , to explore if this behavior can be rationalized in terms of the KGT model for estimating the tip undercooling and Semiati and Kobryn's Hunt solidification diagram. More detailed analysis of the samples micro-texture will then be discussed to explore if an alternative mechanism can account for difficulties in reconciling this approach to predicting the CET with our observations.

II. EXPERIMENTAL AND MODELING METHODS

A. WAAM Sample Manufacture

Single-track 8-mm-wide Ti64 and Ti6242 WAAM linear wall test samples were deposited on 10-mm-thick Ti64 substrates, using the deposition parameters provided in Table I, with a PWP Viper MC plasma torch and TECARC PLASWELD 400 DC power source, in a globally shielded environment purged with Ar atmosphere to avoid oxidation. The wire feed speed was varied systemically during deposition of a set of simple linear test-wall samples, produced with Ti64 and Ti6242 1.2 mm-diameter wire. The wire feed speeds (WFS) were matched as close as possible with the two different alloy feedstocks, the compositions of which are provided in Table II. The sample coordinate system used throughout is defined as the heat source travel ('welding' or 'wall') direction \equiv WD, the transverse (wall thickness) direction \equiv TD, and the build-height (layer normal) direction \equiv ND.

B. Macro and Microstructure Characterization

Cross sections from the walls were cut in both the WD-ND (centerline) and TD-ND (wall transverse section) planes for metallographic examination, to characterize the β -grain structures in 3D. Metallographic samples for optical microscopy and electron backscatter diffraction (EBSD) mapping were prepared by grinding with a grit size down to 4000 grade SiC

Table I. WAAM Deposition Parameters

WAAM Build Parameters	
Wire Feed Speed	26.7 – 52.9 mm/s (varied per deposit)
Travel Speed	4 mm/s (unless otherwise stated)
Wire Diameter	1.2 mm
Current	108 A
Plasma Gas Flow Rate	0.8 l per min
Argon Shielding Gas Flow Rate	< 1000 PPM

paper, followed by polishing with colloidal-silica containing 5 pct hydrogen peroxide. For optical microscopy, samples were etched in Kroll's Reagent and then imaged using a Zeiss Axio 2 microscope, equipped with automated stage mapping software, to produce stitched high-resolution and large-area macrographs.

EBSD mapping was conducted with a Thermo Scientific Apreo C scanning electron microscope (SEM), equipped with an Oxford Instruments' Symmetry 2 EBSD detector and AZtec acquisition software. Maps were collected using a 51 nA current and 20 kV accelerating voltage with 5 and 15 μ m step sizes for TD-ND and WD-TD maps, respectively, due to the difference in scanned sample areas. EBSD data and maps are presented in inverse pole figure (IPF) coloring with the orientation reference parallel to ND. Low (> 5 deg) and high-angle (> 15 deg) grain boundaries (LAGBs and HAGBs) are depicted in the maps as white and black lines, respectively. Reconstructed β -phase EBSD maps were produced from the acquired α -phase orientation data using software developed by Davies and Wynne^[50,51] with up to a 3 deg divergence from the BOR considered part of the same β grain, and a maximum 2 deg misorientation from a particular α variant being accepted. β -grain sizes and aspect ratios were measured from the reconstructed EBSD maps using either a fitted-ellipse major axis or an equivalent circle diameter in AZtecCrystal. To produce β grain misorientation frequency plots (binned every 0.1 deg), data were exported as pixel-to-pixel misorientations, with misorientations < 5 deg filtered out to exclude intra-grain misorientations and reconstruction errors. Twin boundaries were highlighted in β -phase EBSD maps using the *Special Boundaries* feature in AZtecCrystal, where the angle-axis pair misorientations used are stated in each dataset figure. Texture data are presented in contoured pole figures scaled in multiples of random density (MRD).

C. Solidification Modeling

Two classical models were combined to estimate the CET in Ti64: the Kurz–Giovanola–Trivedi (KGT) model,^[47] which was applied to estimate the dendrite-tip undercooling; and the Hunt CET model which was used to calculate $\log(G_L)$ vs $\log(v)$ solidification maps.^[26] The results were then correlated to computational fluid dynamics (CFD) simulations for the above deposition

Table II. Composition in Wt. Pct of the Alloy Feedstock Wires (as Quoted by the Manufacturer)

	Al	Sn	Zr	Mo	V	Si	Fe	N	O	Ti
Ti64	6.14				3.94		0.18	0.008	0.15	bal.
Ti6242	6.00	2.00	3.90	2.00		0.09	0.03	0.003	0.12	bal.

conditions, which were used to estimate the thermal gradients and solidification velocities in the melt pool at the fusion boundary, to determine whether the CET should be theoretically possible with the build conditions employed.

The KGT model^[47] estimates the undercooling of an isolated dendrite growing at a state of marginal stability. The model considers the solutal (ΔT_C) and curvature (ΔT_R) contributions to the dendrite-tip undercooling, ΔT_D , as they are dominant in alloy solidification at moderate growth rates below the conditions of absolute stability:

$$\Delta T_D = \Delta T_C + \Delta T_R \quad [1]$$

For a parabolic dendrite tip growing under steady-state conditions, Ivantsov's solution for solute transport is employed^[52,53] to determine ΔT_C , while also accounting for undercooling *via* the Gibbs–Thomson effect.^[23] The model formulation is described in detail in References 47, 53 and gives a relationship between the tip undercooling, Peclet number, and dendrite-tip radius, which can be expressed as

$$\Delta T_D = m_l C_0 \left(1 - \frac{1}{1 - (1 - K) \text{Iv}(P_c)} \right) + \frac{2\Gamma}{R}, \quad [2]$$

where R is the tip radius, $P_c = Rv/2D$ is the solutal Peclet number, m_l is the slope of the liquidus line on the equilibrium phase diagram, C_0 is the nominal solute concentration, K is the partition coefficient, Γ is the Gibbs Thomson coefficient, and $\text{Iv}(P_c)$ is the Ivantsov solution for the steady-state diffusion field at a parabolic dendrite tip, given by

$$\text{Iv}(P_c) = P_c e^{P_c} \int_{P_c}^{\infty} \frac{e^{-s}}{s} ds \quad [3]$$

Since P_c is itself dependant on R , an additional expression for R based on marginal stability is used^[54]:

$$R = 2\pi \sqrt{\frac{\Gamma}{\sigma^* m_l G_c \zeta_c}}, \quad [4]$$

where G_c can be estimated as the 1D (constitutional) solute gradient^[55]:

$$G_c = -\frac{(1 - K)C_0 v}{D(1 - (1 - K)\text{Iv}(P_c))} \quad [5]$$

And^[47]

$$\xi_c = 1 - \frac{2K}{\sqrt{\left(1 + \frac{2\pi}{P_c}\right)} - 1 + 2K} \quad [6]$$

where v is the dendrite-tip velocity, σ^* is an alloy-dependent dendrite-tip selection parameter that is taken to be a value of $1/4\pi^2 \approx 0.025$, assuming marginal stability.^[56]

Numerical methods are required to solve the tip diffusion field Ivantsov function (P_c) and determine the undercooling for a given solidification velocity. Curve fitting can then be used to obtain a more efficient description of the variation of tip undercooling in response to the solidification velocity.^[57] To estimate ΔT_{dt} , Ti64 was treated as a pseudo-binary system, with respect to Al, using the parameters in Table III, with the liquidus slope calculated by ThermoCalc^[58] for a fixed V concentration. Al was chosen as the solute, as although its partitioning is also weak, it is comparatively stronger than for V ($k_V \sim 0.97$) and has a higher concentration. (Note: for the WAAM process, the effect of non-equilibrium interfacial conditions during rapid solidification on the partition coefficient^[59] is negligible within the solidification velocities used in this study (< 5 mm/s) and the velocity would need to be increased by ~ 10 times before significant solute trapping occurs). The equations above were then solved numerically using the bisection method, as detailed in Reference 60, to obtain a polynomial relationship between tip undercooling and tip velocity.

$$v_{tip} = C(\Delta T)^m \quad [7]$$

In the WAAM process, the tip-solidification rate under steady-state conditions can also be related to the travel velocity of the melt pool, v_p , by Reference 24:

$$v_{tip} = v_p \cos \emptyset, \quad [8]$$

where \emptyset is the angle between the growth vector (melt surface normal) and the melt-pool travel directions. This angle will vary as the angle of the melt-pool boundary changes, reaching a minimum at the center of the trailing edge at the melt-pool surface, and reaching 90 deg at the lowest point in the melt pool where the boundary is horizontal.

The Hunt model^[26] describes the CET by considering competition between columnar and equiaxed growth in an undercooled liquid. It provides analytical expressions for the critical thermal gradient at which the rate of nucleation of new grains exceeds the rate of growth of existing grains, leading to the formation of equiaxed grains ahead of a growing columnar front. Extended

Table III. Parameters Employed in the KGT Model

		Ti-(6Al)-4V	Ti-6Al-(4V)	Ti-Fe	Unit	References
K	partition coefficient	1.15	0.97	0.461	—	[4, 58]
m	liquidus slope	3.308	- 3.688	- 0.15.727	K/wt pct	[58]
C_0	nominal composition	6	4	2.7	wt pct	—
Γ	Gibbs Thomson coefficient	1.88e-7	1.88e-7	1.88e-7	K m	[61]
σ	Surface energy	0.121			J m ⁻²	[62]
D_l	diffusion coefficient in liquid at T_m	6.62e-9	8.17e-9	1e-8	m ² s ⁻¹	[63, 64]
σ^*	dendrite-tip selection parameter	0.025	0.025	0.025	—	[47]

volume fractions of 1 and ~ 50 pct of equiaxed grains are then used to define the boundaries for mixed and equiaxed microstructures, respectively, as

$$G_{\text{columnar}} = 0.617(100N_0)^{1/3} \left(1 - \frac{(\Delta T_N)^3}{(\Delta T_D)^3} \right) \Delta T_D \quad [9]$$

$$G_{\text{equiaxed}} = 0.617N_0^{1/3} \left(1 - \frac{(\Delta T_N)^3}{(\Delta T_D)^3} \right) \Delta T_D \quad [10]$$

which are dependent on the density of nucleation sites (N_0), the critical undercooling for nucleation (ΔT_N), relative to the dendrite-tip undercooling (ΔT_D), determined by the KGT model in response to the solidification velocity (Eq. [8]).

D. CFD Process Model

To estimate G_L and v , simulations are required that include convective flow in the melt pool. A CFD model developed by Chen *et al.* was therefore used to estimate the effect of the wire feed speed on the melt-pool fusion boundary surface and solidification conditions. The model is described in detail elsewhere.^[65–68] In summary, the model considers the liquid metal as a laminar-Newtonian incompressible fluid and uses the volume of fluid (VOF) method to track the time-varying liquid–gas interface (free surface).^[66] The enthalpy-porosity technique was used to implicitly track the time-dependent liquid–solid interface (mushy zone).^[67] The movement of the feed wire was described using mixture theory and the Euler method.^[68] Complex interactions between the feed wire, arc irradiation, pressure, and melt pool (or substrate) have been described through a bespoke surface heat source model and arc-pressure model, described in References 65–68. Detailed information on the wire feeding model, boundary conditions, and numerical methods can be found in the literature.^[65] The simulations were conducted using the same process parameters as those in the experiments. However, to save calculation time, only one deposition layer was modeled on a pre-deposited wall with a height of 15 mm, where the thermal simulated process was assumed to be in a quasi-steady state and independent of the wall height. The bead cross sections of the deposited walls with different WFSs were defined based on experimental results.

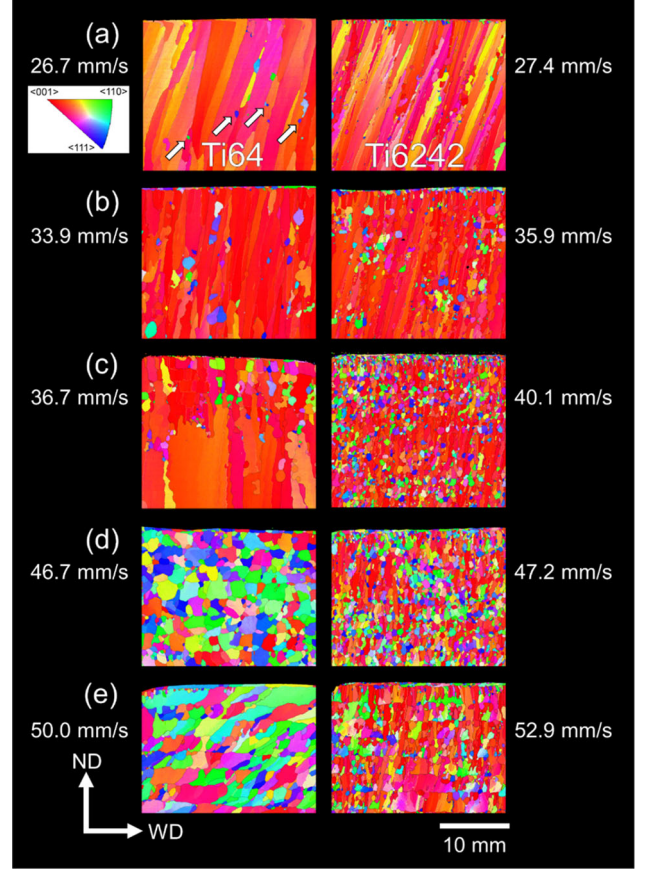


Fig. 1—Reconstructed β phase EBSD maps of the Ti64 (left) and Ti6242 (right) WAAM samples deposited with increasing wire feed speeds (indicated on the far right). The EBSD maps are from the ND-WD plane, taken from the walls' centerline. Island grains are indicated by the arrows in (a). Note also the thin layer of refined grains seen on the top of the final layer on each sample.

III. RESULTS

A. Increasing Wire Feed Speed WAAM Experiments

In parallel work on WAAM process development with a conventional plasma-arc system,^[48] it was not found possible to change the primary β grain structure from columnar to equiaxed by increasing the travel speed, within the limits of the currently available stable process window (which is 3 to 6 mm/s). The approach of increasing the WFS (within the available stable process window) to effect a CET was thus

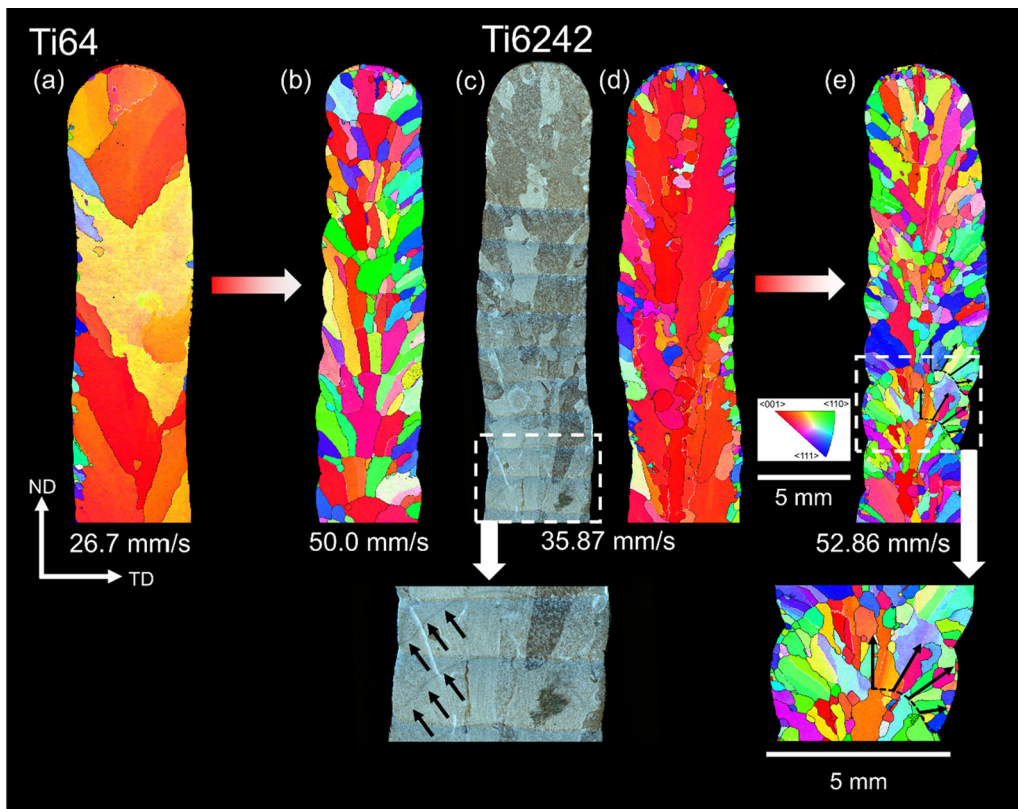


Fig. 2— β -reconstructed EBSD maps of the (a, b) Ti64 and (d, e) Ti6242 WAAM samples deposited with low and high wire feed speeds, below and above the grain structure transition, shown in the ND-TD plane from wall cross sections. Note the fine skin grains seen in the low wire feed speed maps at the wall surfaces. An additional etched optical macrograph has been provided in (c) of the Ti6242 sample to highlight the profile of the fusion boundaries.

adopted here, based on the success of an earlier study performed by Wang *et al.*,^[39] where it was proposed that by increasing the WFS with a constant heat input and travel speed the greater volume of new material melted would decrease the ‘specific energy density,’ so that the melt pool would become cooler, and this would reduce the thermal gradient in the liquid at the solidification front. Theoretically, this would be expected to reduce G_L and lower the G_L/v ratio, thereby promoting solidification conditions that favor nucleation of new β grains ahead of the solidification front.^[25,46] The effect of repeating this experiment and progressively increasing WFS with two titanium alloys, Ti64 and Ti6242, is shown here in greater detail in Figure 1, using reconstructed EBSD maps of the β -grain structure obtained from large centerline WD-ND wall cross sections. The standard (lowest) and highest WFS samples studied are also compared in transverse ND-TD section views in Figure 2 and the transition in texture is depicted in Figure 3.

These figures demonstrate the beneficial effect of increasing the WFS as it clearly leads to a transition to a smaller, more-equiaxed, grain structure. Although the refined grains are still relatively coarse, having a 0.5–2 mm grain size and an aspect ratio of ~ 1.5 , they are much finer and have a far weaker texture than the original coarse and columnar grains produced with a standard low WFS that are centimeters in scale. The

transition in grain structure occurs relatively abruptly in a narrow range of WFS and slightly earlier in Ti6242 (between 35 and 40 mm/s) than in Ti64 (between 37 and 47 mm/s) with this alloy having a finer refined grain structure. However, the initial columnar grain structures in the low WFS Ti6242 build were also smaller in width and there was an overall tendency for a finer grain structure in this alloy across all the samples. At low WFSs, it is also interesting that some small island grains can be observed in the reconstructed EBSD maps for both alloys (arrowed in Figure 1(a)) that are embedded in the columnar grain structure seen in the center of the walls. These grains also increase in number before the full transition to a finer grain structure occurs. In addition, when viewed in cross section (ND-TD plane) in Figure 2, at low WFS, the deposits for both alloys were found to exhibit a ‘skin’ of smaller grains formed on their surfaces, which was more developed in the Ti6242 alloy. In Figure 1, there is also a thin layer of differently orientated fine grains seen in the ND-WD sections on the top of the last deposition track to solidify. This thin refined layer can be observed for all the WFS except with the slowest in the Ti64 samples (26.7 mm/s). In Figure 2, it can further be seen that the WAAM walls built with low WFS have a lower bead layer height and flatter bead profile, which leads to a smaller curvature between layers and less deviation from an ideally flat build surface. Whereas raising the WFS

increases the layer height and edge curvature of each layer, as seen in Figures 2(b) and (e).

The textures obtained from the EBSD maps in Figure 1 are displayed using $\{001\}_\beta$ pole figures in Figure 3. With a low (standard) WFS, the unrefined columnar grains exhibit a strong $\langle 001 \rangle_\beta$ fiber texture aligned near to ND (Figure 1(a)), as has been previously widely reported.^[7,32,33] Because the translation direction was kept constant when building these samples, the columnar grains in the ND-WD sections are tilted by ~ 10 deg in the direction of heat source travel, and the texture in Figure 3(a) is correspondingly slightly off-axis in the pole figures, being similarly rotated around TD toward WD. With increasing WFS, it can be seen in Figures 3(a) through (d) that the strong $\langle 001 \rangle_\beta$ //ND fiber texture intensity is substantially reduced, from 23 to only 3.5 MRD. This weaker texture (Figure 3(d)) could be considered negligible in intensity since there is no clear preferential grain alignment in the pole figure and the MRD over background value was affected by the low grain-sampling statistics.

The grain size distributions for the Ti64 walls are plotted in Figures 4(a) and (c) and highlight an increase in the fraction of small grains with diameters < 1 mm with increasing WFS. Interestingly, a further increase of WFS from 47 to 50 mm/s, beyond that required for the grain structure transition (which was the highest WFS possible without process instability) resulted in a slight rise in the mean grain diameter to 2.2 mm, and the grain aspect ratio also started to increase again as they became more elongated toward the travel direction (Figure 1(e)). In addition, a weak $\langle 001 \rangle_\beta$ fiber-type texture component re-emerged in the pole figures (Figure 3(e)), which resulted in a slightly higher texture strength of 5.6 MRD.

With the Ti6242 alloy, increasing the WFS from 27 to 47 mm/s also greatly refined the original centimeter-scale columnar β grains (Figures 1(a) through (d)), but to a smaller mean diameter of ~ 0.6 mm, nearly three times lower than that for Ti64 (Figure 4(c)). However, the refined Ti6242 samples still contained regions with small elongated columnar grains that locally exhibited a strong $\langle 001 \rangle_\beta$ //ND fiber texture (red in IPF coloring, Figure 1(d)). This is also apparent in the pole figure in Figure 3(d), where the minimum grain size in the 47 mm/s WFS sample has a greater aspect ratio and texture intensity than the corresponding Ti64 sample of 5.2 MRD. Similar to in the Ti64 samples, for WFS greater than that required to achieve a transition in grain structure, the average grain size for the Ti6242 samples also increased again, but more significantly than for Ti64, from 0.6 to ~ 1 mm, and more regions of fine columnar textured grains with a $\langle 001 \rangle_\beta$ //ND fiber texture were present in the microstructure, so that the texture strength rose to 5.8 MRD as the $\langle 001 \rangle_\beta$ //ND fiber component strengthened in the pole figure (Figure 3).

To better understand the 3D grain morphologies, through-wall thickness TD-ND section views of the reconstructed β grains are provided in Figure 2 for the

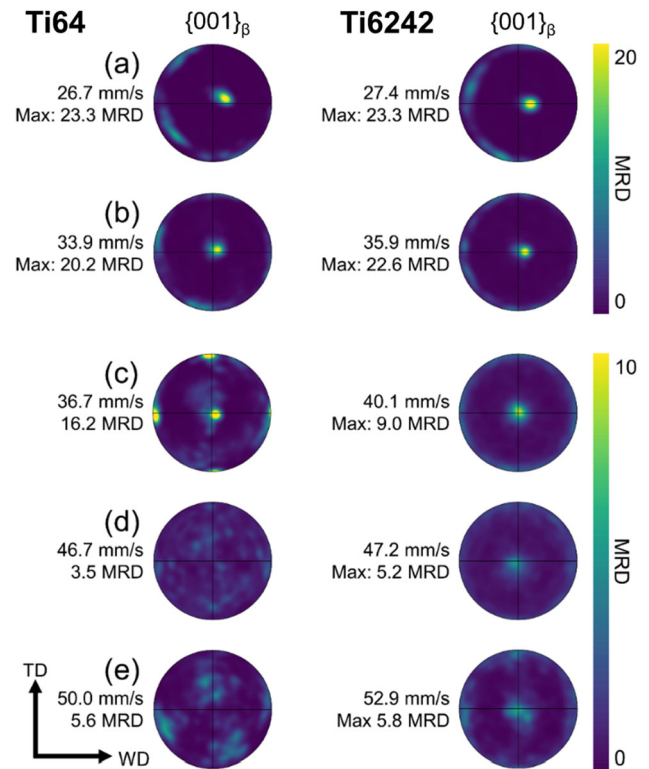
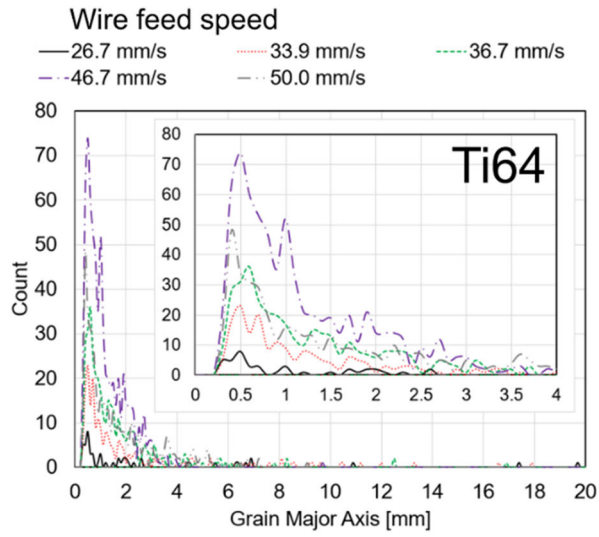
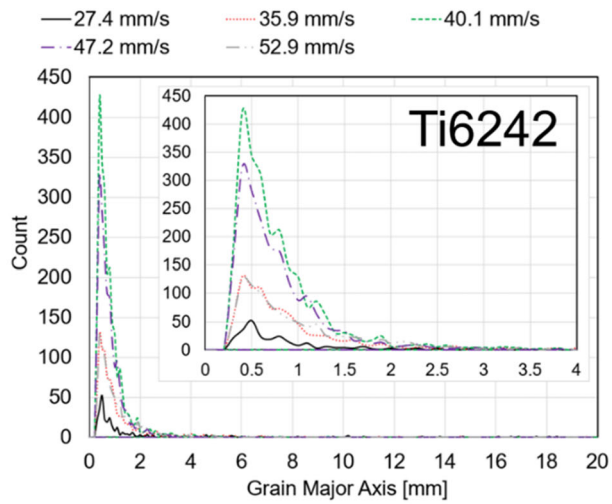


Fig. 3—Pole figures displaying the texture obtained from the reconstructed β phase EBSD maps in Fig. 1, of the Ti64 (left) and Ti6242 (right) WAAM samples deposited with increasing wire feed speeds. From (c) to (e), the MRD scale range has been increased to better reveal the much weaker textures found at high WFSs in the contoured pole figures.

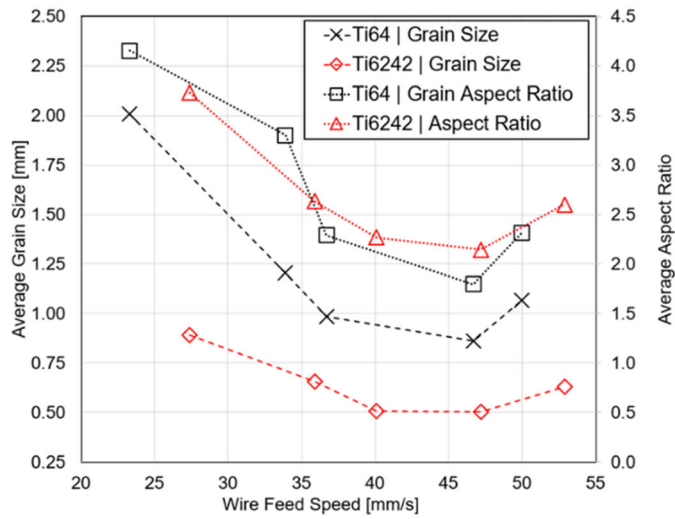
standard low WFS (27 mm/s) and the highest WFS (50 mm/s) samples. In Figure 2(c), an optical image of the Ti6242 cross section is also presented to highlight the fusion boundary profiles of each added layer. This was achieved by etching the stronger transient chemical segregation present at the fusion boundary in this alloy than in Ti64^[4] (arrowed in the magnified section). For the Ti64 sample produced with a low WFS (Figure 2(a)), when observed in this plane, the columnar grains are several millimeters wide and are trying to tilt outwards toward the wall's surfaces. In some cases, the EBSD maps indicate splitting of the growth directions (*i.e.*, the large yellow grain in Figure 2(a) with $\langle 102 \rangle_\beta$ //ND). However, it should be noted that, because the columnar grains are also tilted ~ 10 deg around TD toward WD (Figure 1(a)), the TD-ND cross section cuts them at an angle and their full height cannot be seen in this plane. Following an increase of the WFS to > 50 mm/s, Figure 2(b) further reveals that, although refined and with a far weaker texture, when observed in this orientation, the grains still have a significant aspect ratio and are narrower in TD than in ND and WD, giving them a 'slab-like' cuboidal morphology. Similar to in the Ti64 samples, when depositing Ti6242, raising the WFS further past the transition point from 47 to 53 mm/s (Figure 1(e)) also produced an increase in the average grain size, but unlike in the 50 mm/s WFS Ti64 sample, there was less change in the grain alignment in



(a)



(b)



(c)

◀ Fig. 4—Grain-size histograms of the reconstructed β EBSD maps in Fig. 1 for the (a) Ti64 and (b) Ti6242 WAAM samples deposited with increasing wire feed speeds. In (c), the average grain sizes and average aspect ratios are plotted vs WFS. Fitted ellipse major axes have been used to measure the grain aspect ratio and size. Data below a 200 μm grain size have been filtered out to eliminate reconstruction errors. For the fully columnar structures seen at low WFSs, the grain sizes are underestimated owing to their large size relative to the map area.

the WD-ND plane. However, this was associated with the introduction of some coarser grains of a similar slab morphology to those seen in the Ti64 sample. In addition, when viewed in the TD-ND cross section, the Ti6242 sample deposited with the highest WFS of 53 mm/s (Figure 2(e)) also contained smaller columnar grains with higher aspect ratios with their main grain growth direction rotated away from ND in an arc normal to the curvature of the fusion boundary; *i.e.*, at this WFS, the grain growth directions were strongly influenced by the fusion boundary profile across the breadth of the sample (highlighted in the magnified section in Figure 2(e)).

Finally, from the EBSD IPF maps in Figures 2(a) and (d), it is apparent that most of the small skin grains and island grains seen within the walls produced at low WFS have non- $\langle 001 \rangle_{\beta} // \text{ND}$ orientations. By comparison of the etched image with the EBSD map (Figures 2(c) and (d), respectively), it can further be seen that when viewed in this plane, the preferred growth directions of the skin grains are tilted $\sim 30\text{--}70$ deg away from ND around WD, approximately perpendicular to the curved fusion boundary surface, which is steeply inclined at this position near to the wall's surfaces.

B. CET Predictions

Classical Hunt CET theory is based on the concept of constitutional solute partitioning causing a sufficiently undercooled boundary layer ahead of the solidification front for free nucleation of equiaxed grains in adequate density to cut off columnar growth.^[26] To explore if the Hunt criteria can help understand the β grain transition behavior seen in the AM Ti samples as a function of WFS, estimates were first performed of the dendrite-tip undercooling using the KGT model, which were then used to predict the CET boundaries on a Hunt \bar{G}_L - v solidification diagram, using the relationships described in Section II-C. Figure 5(a) shows a pseudo-binary prediction of the tip undercooling with Al as the main partitioning solute. As the values for liquid diffusivity used in the KGT model are generally poorly known and temperature sensitive, the diffusion coefficient (D_L) for Al at the melting point was taken from first principles molecular dynamics simulations performed by Song *et al.*^[64] and the effect of increasing, or reducing, D_L by a factor of 2 is shown by the dashed lines in Figure 5(a). Altering D_L in this range had a relatively minor influence on the estimated undercooling. Similarly, the solid-liquid interfacial energy was taken from the molecular dynamics simulations performed by Rozas

et al.,^[24] although the ΔT_R had only a small effect on the overall tip undercooling (Figure 5(a)). More importantly, with the 4 mm/s travel speed employed, which will equate to a solidification velocity of less than 4 mm/s, the maximum total predicted dendrite-tip undercooling was less than ~ 1.8 K. Furthermore, the predicted undercooling does not change greatly in the velocity range currently accessible with the plasma-WAAM process. For example, more than doubling the maximum solidification velocity to 10 mm/s is only predicted to increase the undercooling to ~ 2 K.

Due to its much lower partition coefficient compared to Al and V, the effect of Fe ($k_{\text{Fe}} = 0.38$),^[4,21,22] which is a trace addition in Ti64, was also considered with the KGT model and the results are plotted in Figure 5(b). For the normal range of Fe present in Ti64 of $\sim 0.15\text{--}0.2$ wt pct, this produced a smaller tip undercooling than for Al of ~ 1 K, owing to the low Fe concentration. However, as can be seen from Figure 5(b), when the Fe level is increased, this rapidly leads to a large rise in the predicted undercooling. Interestingly, with a blown powder laser DED-AM process, Welk *et al.*^[69] have demonstrated experimentally that systematically increasing the concentration of Fe gave rise to an observable CET at about 2.7 wt pct. This result can therefore be used to provide a rough calibration point for the relative tip undercooling predicted by the KGT model that can induce sufficient free nucleation of new β grains in a Ti alloy to disrupt columnar growth, which from Figure 5(b) can be seen to be $\Delta T_N \sim 8$ K, for a solidification velocity of ~ 5 mm/s.

To apply the estimated dendrite-tip undercoolings predicted by the KGT model in the Hunt model, the critical activation undercooling and heterogeneous nucleation site density are required, which are difficult to obtain directly and these parameters are normally fitted through matching simulated grain structures to experiments (*e.g.*, References 28, 70, 71). In Ti alloys, the nucleation site efficiency and density are particularly poorly known as there are no artificial inoculants. Figure 6 therefore shows an array of Hunt maps^[26] that predict the theoretical transition between columnar and equiaxed solidification regimes using a range of nucleation parameters commonly quoted in the literature, with site densities (N_0) of 10^7 to 10^{14} m^{-3} and activation undercoolings of 0.65, to 7 K.^[72-74] The CET curves from the Semiatin-Kobryn Hunt map are also compared in Figure 6, reproduced from their paper.^[46] These curves have been fitted to experimental data with a different exponent to Eq. [3] ($m = 2$), which gives a shallower slope in the log plot. Nevertheless, agreement with the experimentally fitted curves is only obtained with a very low nucleation undercooling of ~ 1 K and a high site density of 10^{14} m^{-3} . In comparison, from fitting casting simulations to Ti64 and CPTi measured grain structures, activation undercoolings are more commonly reported to be in the range of 4–10 K, with site densities in the range of 5×10^7 to 2×10^9 m^{-3} .^[72-74]

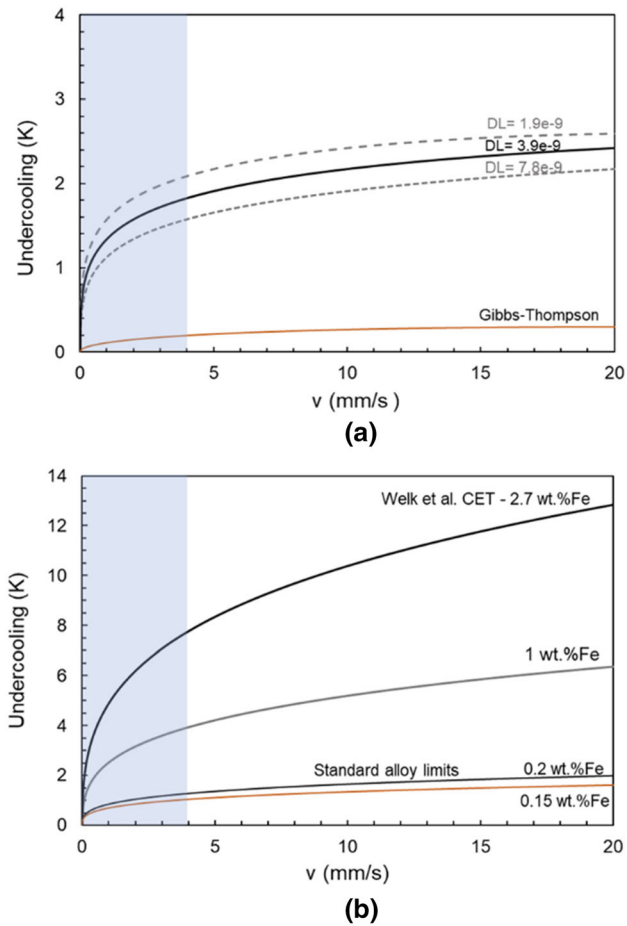


Fig. 5—Dendrite-tip undercoolings predicted from the KGT model, as a function of solidification velocity: (a) treating Ti64 as pseudo-binary with respect to Al, showing the solutal and Gibbs Thomson contributions ΔT_C , ΔT_R , and (b) showing the effect of Fe on the tip undercooling of a Ti-Fe binary alloy. The shaded region indicates the solidification velocity range in the current experiments, which range from 4 mm/s at the center of the trailing edge of the melt-pool surface, to 0 mm/s at the bottom of the melt pool according to Eq. [8]. The dashed lines in (a) indicate the effect of changing D_L ($m^2 s^{-1}$) by a factor of 2, to show the effects of uncertainty in the value of D_L which is inherently difficult to measure.

C. Predicted Solidification Conditions

The CFD model developed by Chen *et al.*^[65–68] was used to estimate the effect of the wire feed speed on the melt-pool shape and solidification conditions. Centerline sections from this model are presented in Figure 7, parallel to the travel direction, along with the average liquid thermal gradient, G_L , and growth velocity, v , normal to the solidification front estimated along the rear section of the melt pool, which experiences the most favorable conditions for grain nucleation (*i.e.*, the lowest ratio of G_L/v). The positions over which G_L and v were averaged are indicated by the dashed line in figure. Figure 7(a) reveals that as the WFS is increased, the bead height also increases, but the melt-pool volume and temperature distribution do not change dramatically because, with the same energy input and travel speed, this is mostly compensated for by a reduction in the

remelt depth (Table IV). Overall, this leads to a relatively small effect on G_L , which can be seen in Figure 7(b) to reduce only from $\sim 1 \times 10^6$ to 0.7×10^6 K/m when the WFS is increased from 26 to 50 mm/s. However, the rising bead height with WFS notably changes the melt-pool shape and fusion boundary profile, which becomes more tilted toward the travel direction. Overall, this increases the angle of the fusion boundary relative to the travel direction (WD) at the rear of the melt pool, which has a small effect on increasing v in the upper section of the melt-pool rear where grain refinement is most likely to occur from about 2 to 3.5 mm/s. The effect of increasing wire feed speed on simulated remelt depth, and experimentally measured layer height and bead width (curvature) for the Ti64 samples are summarized in Table IV. It should be noted that increasing the wire feed speed also increases the curvature of the bead profile in the ND-TD cross section, as can be seen from the change in bead height-to-width ratio.

In Figure 8, the values of G_L and v , estimated from the CFD melt-pool simulations, are plotted on an enlarged region of the experimental Hunt diagram proposed by Kobyn and Semiatin,^[46] which has been replotted along with their experimental data points. It can be seen that the estimated values of G_L and v from the WFS experiments are all grouped in a narrow range above the columnar-equiaxed transition lines, within the columnar region of the solidification diagram, and with increasing WFS the liquid thermal gradient does not change sufficiently to cross the CET lines.

D. Evidence for Dendrite Twinning

Since the above simulations point toward an alternative mechanism being responsible for the grain structure transition seen in the WFS experiment, other than the free nucleation of new dendrites ahead of the solidification front, the reconstructed EBSD maps in §3.1 were analyzed in more detail. If the refined grains were produced by free nucleation in the liquid they would not be expected to share an orientation relationship with each other, and the grain misorientation frequency plots obtained from the samples would be expected to exhibit a random Mackenzie distribution.^[75] Pixel-to-pixel misorientation distributions were therefore produced from the EBSD data, which are depicted in Figure 9. With the lowest WFS (< 36 mm/s) samples, which have coarse, textured, columnar grain structures, peaks in misorientation frequency are seen from their mutual low-angle grain boundaries (LAGBs) of ~ 10 and 17 deg. By examination of the EBSD maps, these misorientations were confirmed to be produced by grain boundaries between the $\langle 001 \rangle_{\beta}/ND$ fiber textured columnar grain trunks. For the Ti6242 samples, the ~ 10 deg peak was much stronger, owing to the propensity for this alloy to form thinner columnar grains with low misorientations, due to greater growth restriction from the partitioning of Mo, Zr, and Si.^[21,22,76,77] However, as the WFS for both Ti64 and Ti6242 increased, the LAGB peaks associated with the

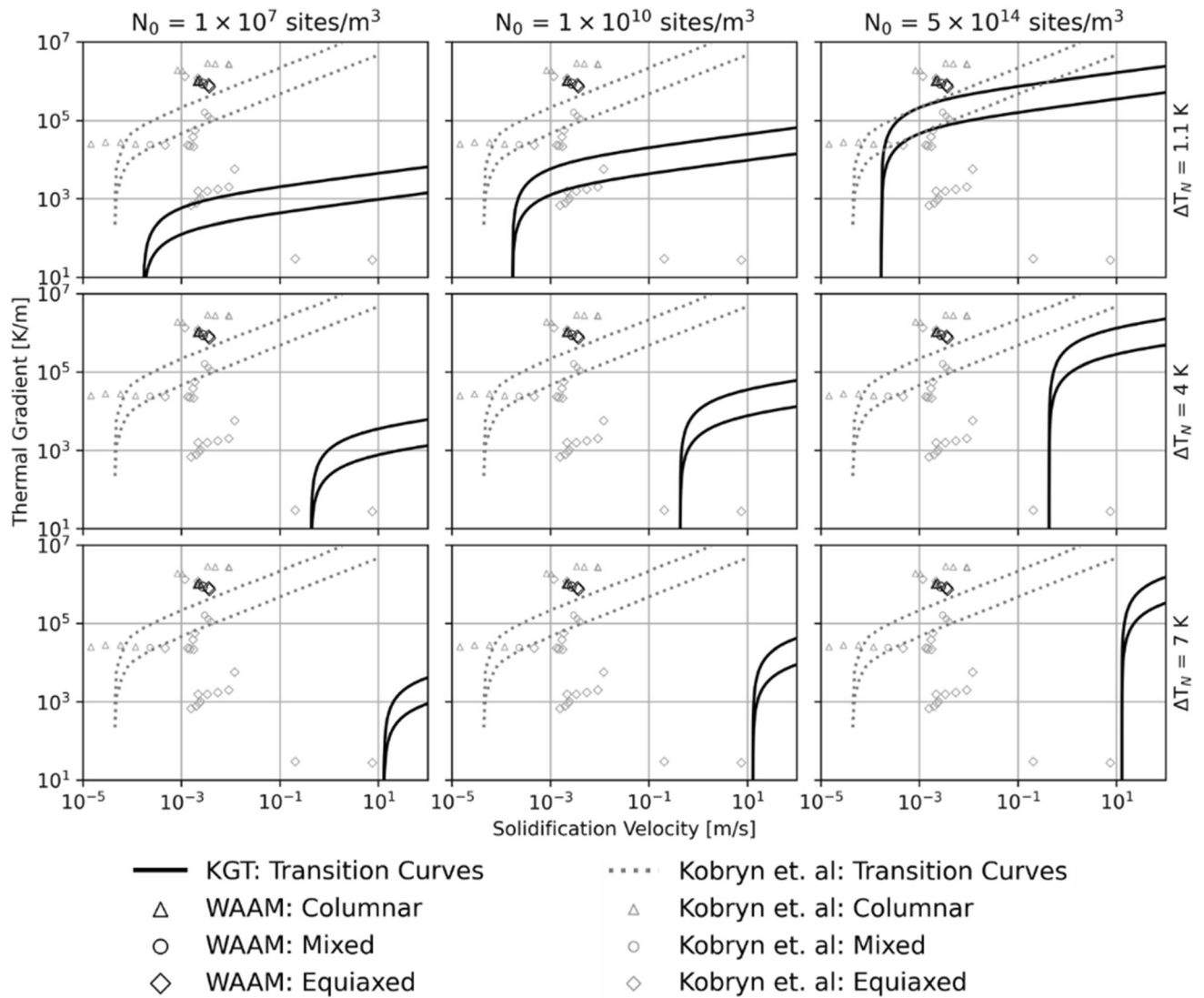


Fig. 6—Hunt maps^[26] employing the pseudo-binary KGT model for Ti64 with respect to Al, showing the predicted theoretical transition between columnar and equiaxed solidification regimes in response to the liquid thermal gradient and solidification front velocity. An array of nucleation parameters have been investigated, with nucleation site densities (N_0) of 10^7 sites/m³, 10^{10} sites/m³, and 10^{14} sites/m³; and activation undercoolings of 0.65 K, 4 K, and 7 K. Curves fitted to a range of experimental data by Semiatin and Kobryn are included for comparison^[46].

columnar grains reduced to be replaced by two high-angle grain boundary (HAGB) misorientation peaks, concentrated at 51 and 60 deg. These peaks, formed by a 51 deg rotation around $\langle 110 \rangle_\beta$ and the much stronger peak by 60 deg around $\langle 111 \rangle_\beta$, correspond closely to the two Ti- β twinning systems possible in BCC metals; $\{332\}_\beta \langle 113 \rangle_\beta$ and $\{112\}_\beta \langle 111 \rangle_\beta$, respectively.^[78,79] The area fraction of boundaries with these twin misorientations is also presented in Figure 9(c) plotted against WFS where they can be seen to reach a high level of ~ 21 and 27 pct in the most grain-refined conditions in the Ti6242 and Ti64 alloys.

Boundaries with these misorientations have been defined in the EBSD maps shown in Figure 10 for the samples produced with the lowest and highest WFS of ~ 47 mm/s. Maps are provided with ± 5 and 10 deg deviations from the ideal twin relationships, to allow for reconstruction and measurements errors. However,

there is little difference between the fractions of twin boundaries identified. Original IPF texture maps are also included in Figure 10 for comparative purposes. It was noted above that in Figure 1(a) the coarse and columnar grain structures present at low WFSs contained a small volume fraction of low-aspect ratio island grains, which are enlarged in Figure 10(c). In the accompanying twin boundary maps, it is apparent that these smaller grains all have at least one boundary that has partial, or in many cases full, twin character. In the post-transition, high WFS samples where finer grains dominated the microstructures many, but not all, of the grains also exhibit twin boundaries, as can be seen in Figures 10(b) and (d). For this high WFS condition, where there is an aggregate of more equally sized grains, a 2D section cannot determine all the possible neighboring grain orientation relationships. Nevertheless, the fraction of twin boundaries is still very high

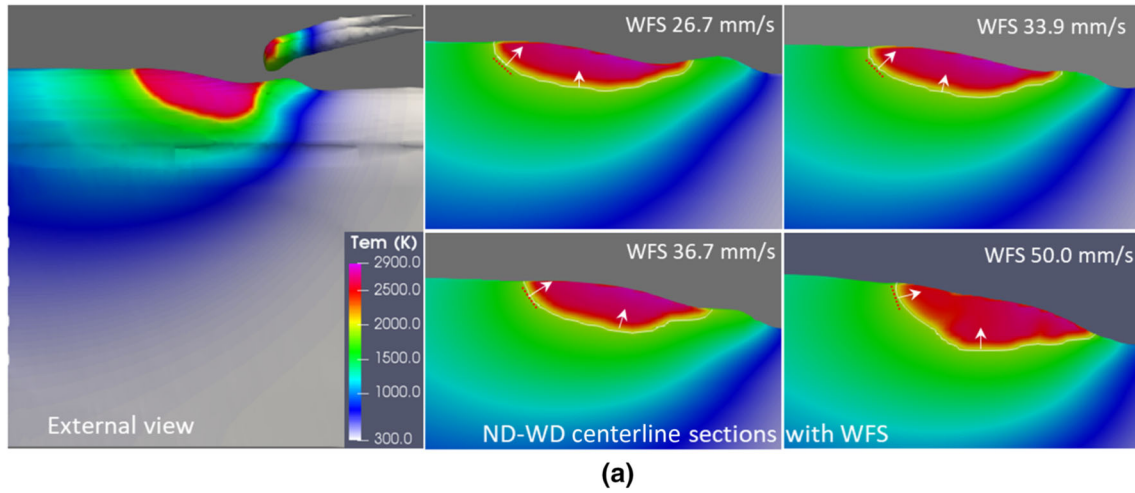


Fig. 7—CFD melt-pool model predictions showing the effect of wire feed speed (WFS) on (a) the melt-pool centerline profile, parallel to the travel direction, and (b) the liquid thermal gradient, G_L , and estimated average growth velocity, v , normal to the solidification front at the rear section of the melt pool.

(Figure 9(c)). Overall, these results therefore strongly suggest twinning is involved in the grain structure transition seen in Figure 1 during WAAM with increasing WFS.

IV. DISCUSSION

A. Solidification Conditions

Predictions of the CET in metal alloys are notoriously difficult due to a poor knowledge of the critical undercooling for nucleation (ΔT_N) and the heterogeneous site density (N_0), as well as important physical parameters such as the diffusivity in the liquid (D_L) and the interfacial energy (σ). In Ti alloys, this is compounded by the fact that nucleation in the melt occurs ‘naturally’ without the benefit of artificial inoculants, so that the efficiency and the density of the nucleating particles is largely unknown and will be highly dependent on the processing conditions. While estimates made using the KGT model are therefore not likely to be highly accurate in absolute terms, they do reflect the low level of solute partitioning that occurs in Ti64, which

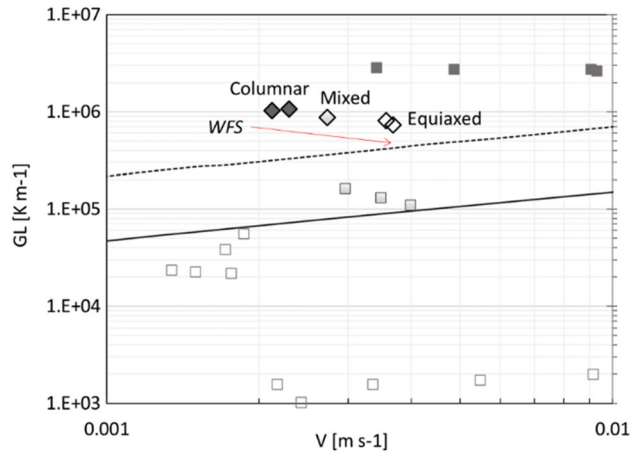


Fig. 8—Average values of G_L and v from the CFD simulations (labeled ‘WFS’), estimated at the solidification front at the rear of the melt pool, shown on the replotted Hunt diagram proposed by Kobayashi and Semiatin,^[46] along with their experimental data points.

leads to predictions of a dendrite-tip undercooling of less than 2 K (~ 1.8 K) at relatively high solidification velocities compared to casting conditions of $v \sim 2$ to

Table IV. The Effect of Increasing Wire Feed Speed During Deposition of Ti64 on Simulated Remelt Depth (This Work, Fig. 8a), and Experimentally Measured Layer Height and Bead Width (as Recorded in the Previous Study in Ref. [49]).

Wire Feed Speed (mm/s)	Layer Height (mm)	Bead Width (mm)	Remelt Depth (mm) (CFD Data)
26.7	1.1	7.2	0.8
33.9	1.6	7.2	0.5
36.7	1.7	6.8	0.4
46.7	2.4	6.8	0.1
50.0	2.5	6.7	0.1

4 mm/s. Here, we have not used the same approach with the Ti6242 alloy because there is greater uncertainty in applying a pseudo-binary KGT model to this more complex alloy.

Although the CET can be achieved in aluminum alloys that employ highly efficient TiB₂/Ti grain refiners at such low undercoolings,^[27,78] when compared to a laser powder DED-AM experiment performed by Welk *et al.*^[69] who increased the concentration of Fe, which partitions much more strongly than Al, until a CET was observed at 2.7 wt pct, the KGT model predicted a tip undercooling of $\Delta T_D \sim 8$ K (at $v = 5$ mm/s). While these predicted absolute values are subject to some uncertainty, by comparison, this suggests that without the use of artificial inoculants, the relative undercooling calculated for Ti64 is normally too low for sufficient free nucleation to occur in the liquid in DED-AM process to cut off columnar growth. Furthermore, other simulations of cast grain structures in CPTi and Ti64 have fitted experimental data with similar critical nucleation undercoolings in the range of 4–10 K, and relatively low site densities of 5×10^7 to 2×10^9 m⁻³.^[72–74]

With an efficient nucleant, Greer *et al.*^[80] have proposed that the critical undercooling is determined by the condition for free growth from the inoculating particle, ΔT_{fg} , which scales inversely with the particle diameter according to

$$\Delta T_{fg} = \frac{4\sigma}{\Delta S_V d}, \quad [11]$$

where d is the particle diameter and ΔS_V is the entropy of fusion. Using values for Ti of $\sigma = 121$ mJ m⁻² (determined by molecular dynamics simulations)^[24] and $\Delta S_V \sim 0.63$ MJ m⁻³^[81] gives the diameter of a naturally occurring inoculant, required to be effective at the predicted undercooling of 1.8 K, as 0.5 μ m. Whereas, for an undercooling of 8 K, predicted for a Ti-2.7 wt pct Fe alloy, it would be considerably smaller at ~ 100 nm. Due to its high reactivity, heterogeneous nucleants that are generated naturally in Ti alloys can only come from sources such as oxides, nitrides, or other ceramic particles. Because of their high reactivity with oxygen, Ti alloys are processed under very clean conditions involving vacuum-cold hearth processes and in this experiment WAAM deposition was performed in an Ar purged tent with very little evidence of oxidation on the deposit. Oxide inclusions are also rarely seen in Ti alloys due to their high solubility for oxygen, and carbon also has a high solubility in liquid Ti at the melting point (~ 1.6 at. pct).^[82] It is possible that nitrides

can precipitate from liquid titanium, but this would only occur if there was a severe level of contamination of the liquid.^[35] The density of suitable naturally occurring particles formed by contamination with the environment would therefore be expected to be low. Although grain nucleation from dendrite fragmentation can operate at a negligible undercooling, and it is possible for small, unmelted fragments of the feedstock wire to survive in the melt pool and act as nucleants, these will also be less prevalent in a weakly segregating alloy like Ti64, which will have a very narrow mushy zone and solidify with short, stubby, dendrites. This lack of naturally occurring nucleants explains why such a high undercooling is normally required to cross the CET in Ti alloys.

In addition, the KGT model shows that the dendrite-tip undercooling is not expected to increase quickly with process speed in the range accessible by WAAM deposition; *i.e.*, on doubling the maximum solidification velocity, ΔT_D increased from 1.8 to 2 K. It should be noted that it is important to consider melt-pool convection when predicting the solidification conditions at the fusion boundary. The CFD model showed that increasing the WFS does not change the G_L/v ratio as dramatically as expected because, as more wire is added with the same heat input, this does not cool the melt pool because the process self-compensates by remelting less of the previous layer and the melt-pool volume stays nearly constant. However, this does give rise to a higher and more rounded bead for each melt track and the melt pool becomes more tilted toward the heat source travel direction. When predicted at the fusion boundary by the CFD model, the simulated values of G_L/v only reduced by about a half with increasing WFS (Figure 7) and all the conditions were predicted to be within the columnar region of the experimental Hunt map proposed by Kobryn and Semiatin^[46] (Figure 8). Overall, it therefore seems unlikely that a conventional CET will be accessible in WAAM processes with Ti alloys like Ti64 that have a very low freezing range, by changing the processing conditions within a stable window that still gives acceptable bead geometrical shape, although it has been shown that this can be achieved under the same conditions (*i.e.*, with a $\Delta T_D < 2$ K) by the addition of efficient inoculant particles like TiN.^[35]

B. The Formation of New β -Grain Orientations by Twinning

The fact that both alloys showed a similar response to an increased WFS and contained a high area fraction of grain misorientations consistent with twinning suggests

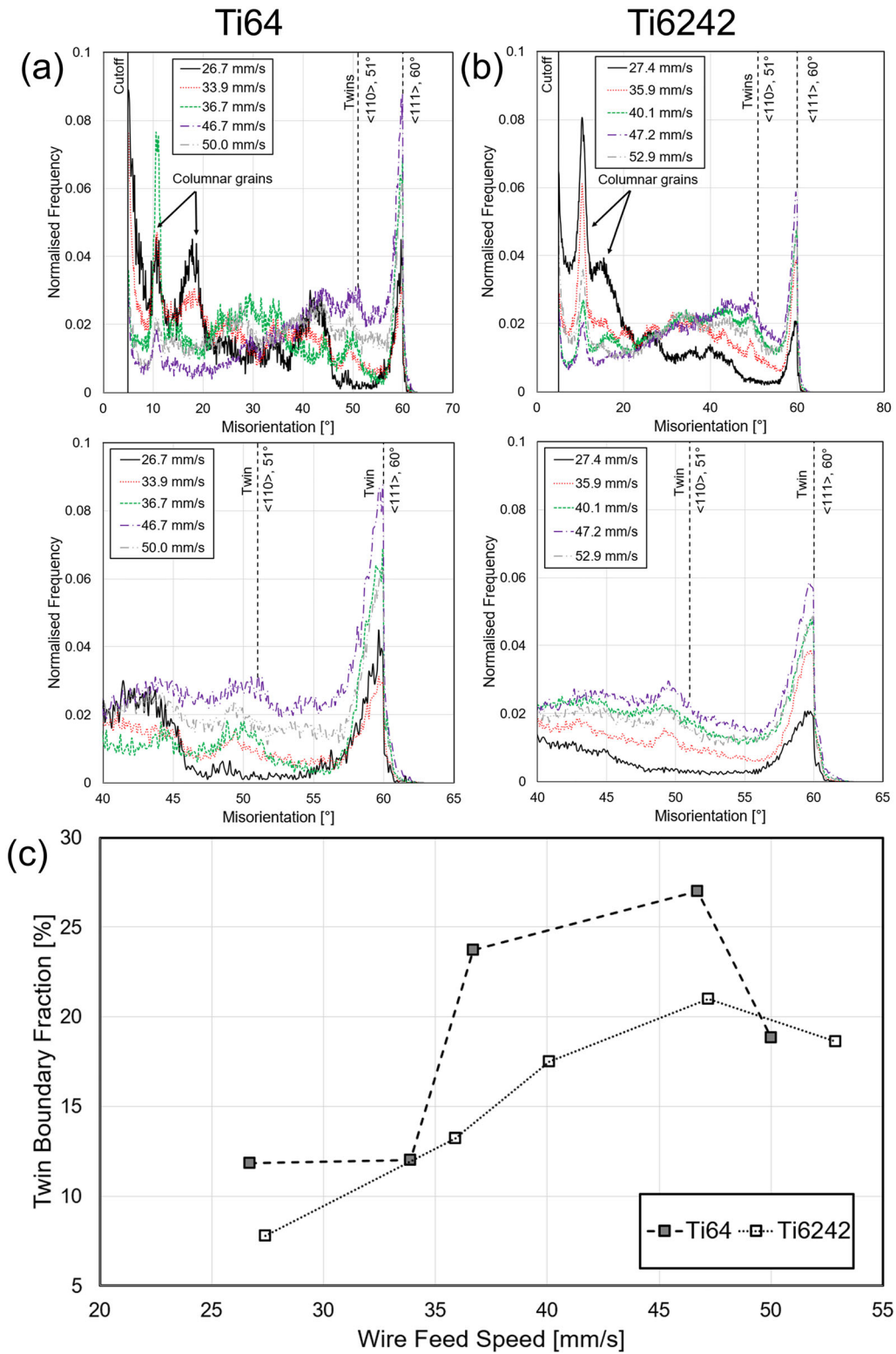


Fig. 9—Pixel-to-pixel misorientation frequency distributions taken from the EBSD data in Fig. 1 of the (a) Ti64 and (b) Ti6242 samples deposited with increasing wire feed speeds. The two common twinning systems in β -phase Ti have been highlighted. Data below a 5 deg misorientation have been filtered out to exclude reconstruction errors. (c) Compiled twin percentage fraction of total grain boundary 'area' plotted against wire feed speed.

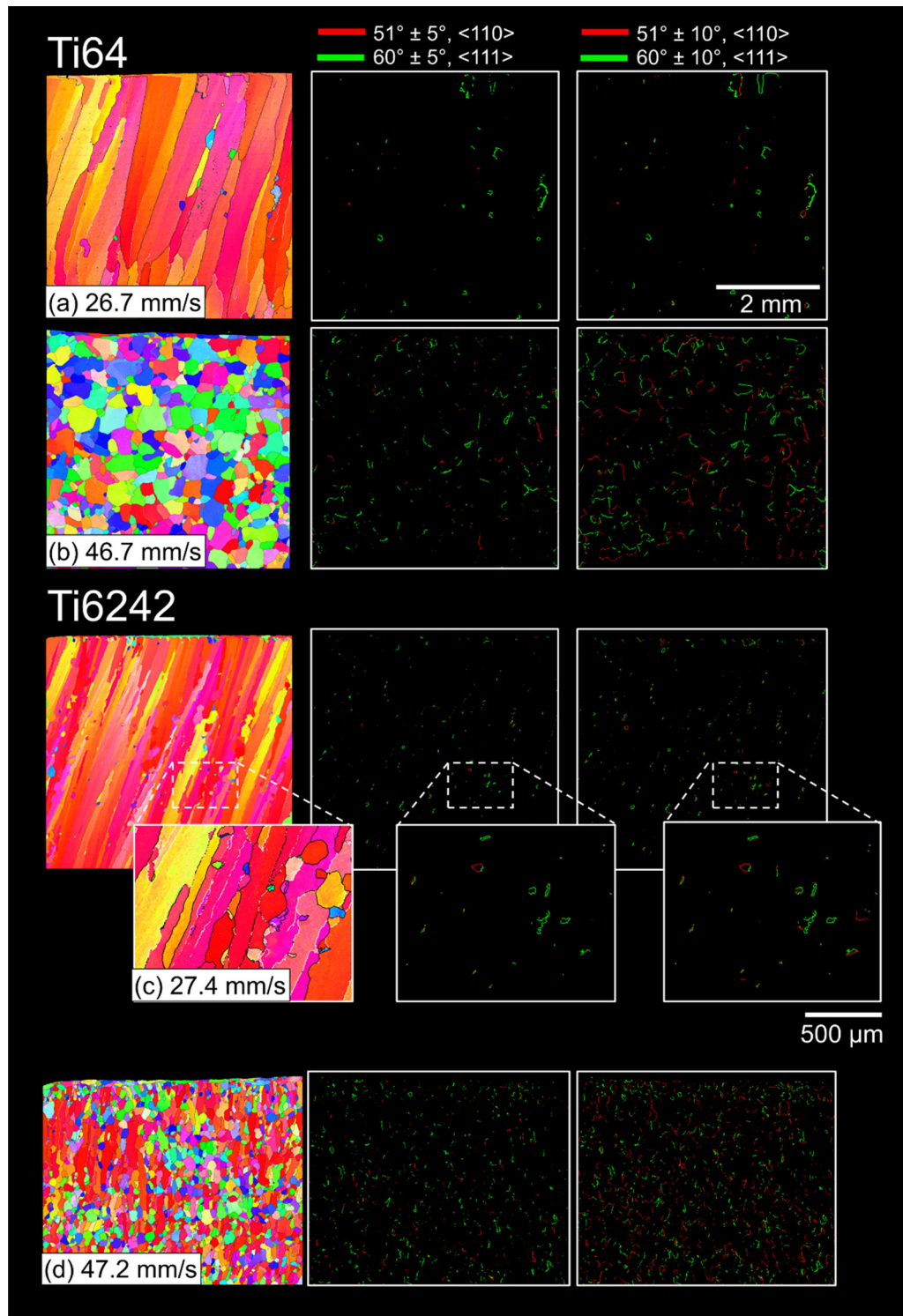


Fig. 10—Reconstructed- β EBSD maps, shown in IPF//ND orientation, with two common β phase Ti twinning boundary relationships highlighted ($51^\circ \pm 5^\circ$ around $\langle 110 \rangle_\beta$ (red) and $60^\circ \pm 5^\circ$ around $\langle 111 \rangle_\beta$ (green)), with deviations of ± 5 and ± 10 deg allowed from the ideal orientations; for (a) the Ti64 and (b) Ti6242 WAAM samples, with low WFSs and columnar and at high WFSs with equiaxed grain structures.

that, without modification, the Hunt model is not relevant to the main mechanism responsible for the grain structure transition observed. Twinning is known to occur during solidification by stacking faults forming during atomic attachment at the solid-liquid

interface.^[83,84] However, twinned grains are only observed in the final microstructure if a twinned dendrite segment gains a growth advantage, so that it is not rapidly overgrown by the original growth direction. In welding, twinned-columnar grains typically

form in elliptical melt pools when dendrites try to adjust to the curvature of the melt-pool surface, which leads to their primary trunks deviating increasingly from the direction of the maximum thermal gradient (normal to the solidification front) as they grow inwards from the fusion boundary.^[25] The dendrite tip and arms will also try to readjust to follow this curvature, but this is crystallographically constrained by planes of preferential atomic attachment that dictate the preferred dendrite crystallographic growth directions (*i.e.*, $\langle 001 \rangle_{\beta}$ for BCC Ti).

Under such conditions, a twinned branch may gain a growth advantage over its parent dendrite and develop into a new grain orientation.^[83,84] In the case of the BCC β Ti phase, this would occur when a twinned $\langle 001 \rangle_{\beta}$ dendrite growth direction becomes more closely aligned with the maximum thermal gradient at the solidification front, \vec{G}_L . For the most commonly observed $\{112\}_{\beta}/\{111\}_{\beta}$ twin, this will reorientate the growth direction by 64 deg. A schematic diagram of this process is provided in Figure 11. To the authors' knowledge, dendrite twinning has not been previously documented in Ti alloys, or in other BCC metals, but it has been studied extensively in aluminum alloys.^[83,84] Previous work on aluminum^[83] shows that twins tend to occur during solidification with high thermal gradients and growth rates (*e.g.*, $G_L > 1 \times 10^3$ K/m, $v > 1 \times 10^{-3}$ m/s); *i.e.*, under similar conditions to in welding and AM. It has been proposed that the growth advantage of twinned dendrites over the original parent trunk orientation is gained primarily by better alignment of the preferred directions with the highest thermal gradient. Interactions with the ejected solute in the parent-twin inter-dendritic regions, and the shape difference of the twinned dendrite tip, can also contribute.^[83,84] Molecular-dynamics simulations have also shown that patches of stacking faults can readily occur during attachment at the solid-liquid interface.^[85] However, for a twinned dendrite to develop from a stacking fault into a grain

that is not overgrown in alloys with low solute partitioning, the growth advantage gained from realignment of a preferred growth direction with the thermal gradient is most likely to dominate.

A good example of this behavior can be seen in the Ti6242 low WFS sample that contained isolated small grains in its center that have been overgrown by the surrounding $\langle 001 \rangle_{\beta}/ND$ large columnar-grained matrix, enlarged in Figure 10(c). For nearly all these island grains, it was possible to identify a twin boundary with the surrounding columnar grains. They were therefore clearly initiated by twinning at the growth front, but this tilted the grains away from $\langle 001 \rangle_{\beta}$ alignment with the maximum thermal gradient vector and they were subsequently overgrown by the more favorably aligned $\langle 001 \rangle_{\beta}/ND$ matrix columnar grains. In Figure 12, the TD-ND cross section EBSD map of the Ti6242 low WFS sample is compared to the location of the 51 deg $\langle 110 \rangle_{\beta}$ and 60 deg $\langle 111 \rangle_{\beta}$ twin boundaries present. Most of these smaller wall surface grains also have twin-type boundaries with the central columnar grains, but not all. This is to be expected because, in a 2D cross section, it is possible for a grain to have its twin boundary out of plane. A similar surface skin of smaller twinned grains also formed on the low WFS Ti64 sample, but they were less developed in this alloy (see Figure 2(a)). In Figure 13, a more enlarged region is shown of a typical skin grain, where its position relative to the fusion boundary has been highlighted by adjusting the contrast in an etched optical macrograph in Figure 13(a). This grain's orientation is displayed in the pole figure in Figure 13(c), where it has a 51 deg $\langle 110 \rangle_{\beta}$ twin relationship with the neighboring $\langle 001 \rangle_{\beta}/ND$ (red) large columnar grain in the wall center, from which it developed. For this example grain near the wall's surface \vec{G}_L will be normal to the curved fusion boundary and is tilted by about 50 deg to ND, in the ND-TD section view, but is also tilted out of plane being rotated about

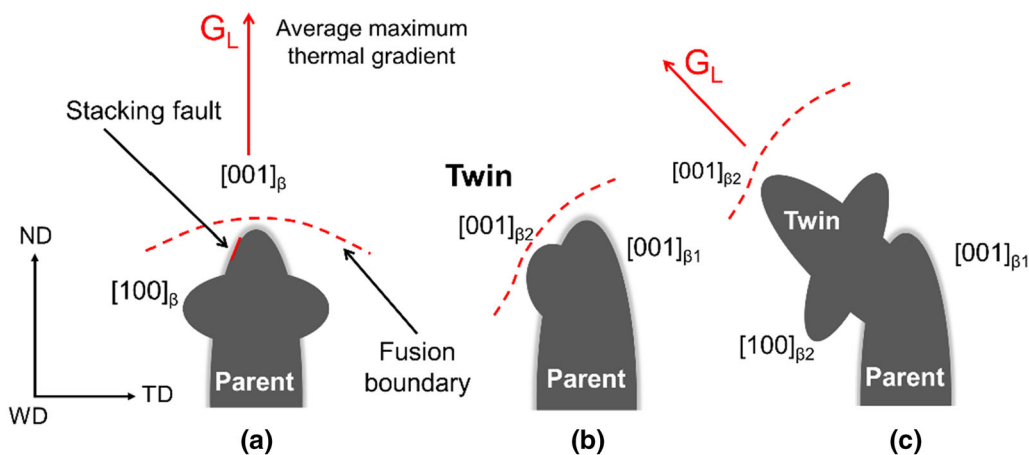


Fig. 11—Schematic of the proposed mechanism of dendrite twinning in WAAM showing: (a) a parent dendrite growing parallel to the maximum thermal gradient at the wall center normal to the fusion boundary (which is not to scale), (b) the formation of a dendrite twin that develops from a stacking fault on the solid-liquid surface at a point on the curved fusion boundary where the twin becomes closer aligned with the maximum thermal gradient, and (c) the more favorably aligned twinned dendrite out-growing and beginning to cut off the original columnar dendrite.

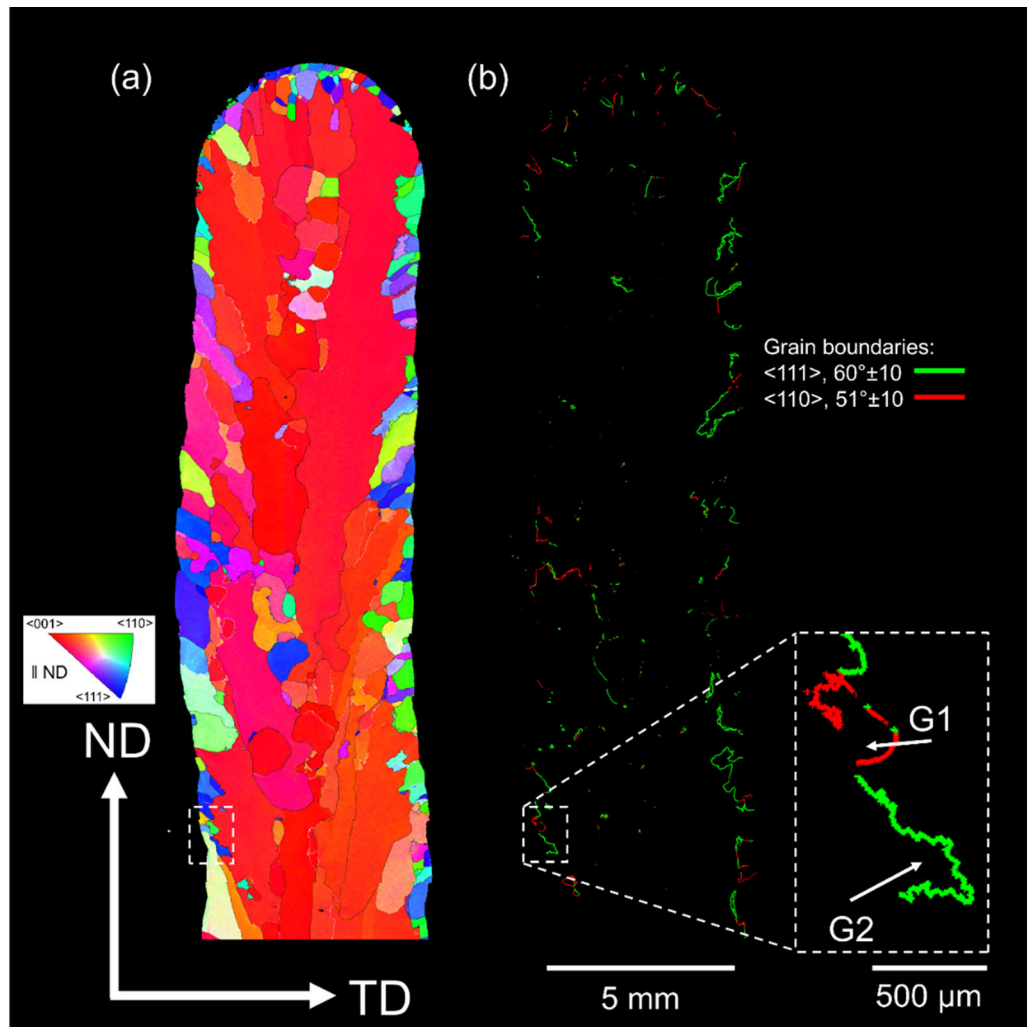


Fig. 12— β -reconstructed EBSD map of the Ti6242 WAAM sample built with a low wire feed speed of 35.87 mm/s in the ND-TD plane showing: (a) an IPF orientation map and (b) the corresponding twin boundaries present. Grains G1 and G2 are examined in more detail in Fig. 13.

TD toward the heat source travel direction by a smaller angle of ~ 10 – 15 deg.

In this transverse section ND-TD view, the maximum thermal gradient (\vec{G}_L) is parallel to ND at the WAAM wall centerline, but progressively tilts further away toward the wall edges, following the curve of the convex fusion boundary. This is in the opposite direction to that seen typically in welding, where a small melt pool is created in a large plate and the fusion boundary has a concave bowl-shaped surface.^[86] In contrast, in WAAM with a single-track-wide wall, because of the different heat-flow geometry with a thin deposit and the curved bead profile from the previous layer, the melt-pool fusion boundary surface is more similar to a ‘saddle’ shape in 3D (compare Figures 7(a) and 13(a)). Due to the convex fusion boundary surface, grains with closest $\langle 001 \rangle_\beta$ alignment to the maximum thermal gradient will also tend to expand sideways and they will overgrow less favorably orientated neighbors, unless this is inhibited by solute segregation, and this process contributes to the formation of the very coarse, columnar, and strongly

textured wall-core grain structures seen in Figure 4(a) at low WFS. Expansion laterally will, however, require branching and adjustment of dendrite side arms, and the greater the curvature, the greater will be the deviation from the primary trunk crystallographic alignment with the solidification front normal.

In the EBSD maps in Figures 2(a) through (d) and 13(a) and (b), it is apparent that when the fusion boundary surface normal deviates too strongly from ND, a transition to a skin layer of smaller differently orientated β grains develops. This transition appears to occur when the deviation angle is greater than about 40 deg (Figure 13(c)). For example, by reorientation, the twinned grain in Figure 13 has a $\langle 001 \rangle_\beta$ crystal direction aligned almost exactly parallel with the fusion boundary normal at this position. Hence, at this point on the fusion boundary, the ~ 40 deg tilted direction of \vec{G}_L created conditions where a stacking fault led to a twin developing with a rotated $\langle 001 \rangle_\beta$ direction that was near to parallel to the maximum thermal gradient at this position. This gave it a large growth advantage so that it

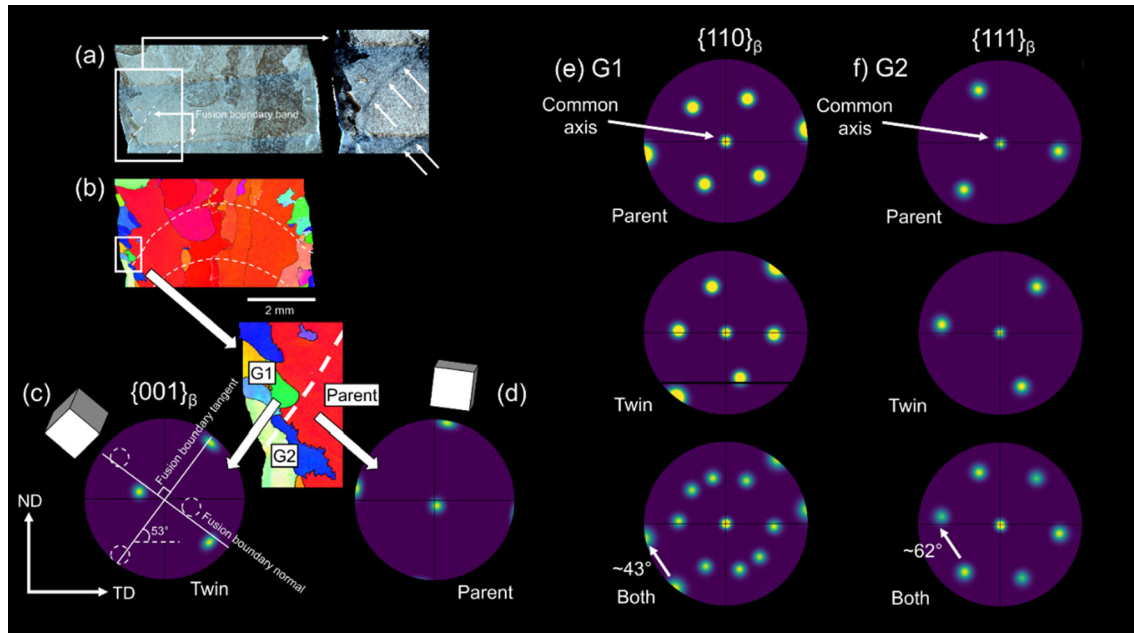


Fig. 13—Analysis of the orientations of the small ‘skin’ grains formed near the wall surfaces in the Ti6242 WAAM sample built with a wire feed speed of 35.87 mm/s: (a) etched optical macrograph showing the fusion boundary curved profile, (b) reconstructed β EBSD map of the same area, with pole figures (c, d) showing the orientation of the twinned grain of interest, compared to that of the neighboring parent columnar $\langle 001 \rangle_{\beta}$ //ND (red) grain, with which it has a ~ 51 deg $\langle 110 \rangle_{\beta}$ twin relationship. (e, f) shows stereographic projection $\{110\}_{\beta}$ and $\{111\}_{\beta}$ pole figures of the parent and twinned grains G1 and G2 (highlighted in (c) and in Fig. 12), both separate and together, orientated parallel to common $(011)_{\beta}$ and $(111)_{\beta}$ directions, demonstrating β -twinning systems.

could develop into a dendrite branch that cut off the original parent $\langle 001 \rangle_{\beta}$ dendrite growth direction orientated close to ND.

C. Transition to a Refined β -Grain Structure

As a WAAM deposit is normally built with multiple layers and a large remelt depth, without the introduction of efficient nuclei, the β grains reformed at the fusion boundary in each pass grow epitaxially into the melt pool. After multiple passes, the wall-core grains are therefore selected with $\langle 001 \rangle_{\beta}$ directions aligned parallel to the average normal to the melt-pool base, which develop into the coarse and columnar grains (Figure 1(a)). With a constant translation direction, grains will be preferentially selected that tilt toward the travel direction as the melt-pool base slopes upwards toward its rear (e.g., ~ 10 deg in Figure 7(a)). The transition to a refined grain structure within the wall cores, which also contains many small grains with twin relationships, can therefore be largely attributed to the effect of the WFS on the melt-pool geometry. This behavior is illustrated schematically in Figure 14. In Figure 7, it can be seen from the CFD simulations that as the WFS increases, the bead height rises and the remelt depth reduces, which increasingly tilts the rear melt-pool fusion boundary surface toward the travel direction. As well as increasing in inclination, there is also predicted to be an increase in depth of the steepest section of the fusion boundary toward the top of the melt pool. As shown in Figure 14, this has the same effect as the melt-pool surface curvature seen in the

TD-ND cross section at low WFS, where the melt-pool base was flatter; i.e., for a larger melt-pool depth, the direction of the maximum thermal gradient at the fusion boundary at the rear of the melt pool in the WD-ND plane tilts more toward WD as the WFS increases. As the angle of inclination becomes more severe, this will again result in twin orientations. These form by stacking faults on the solid-liquid surface having better alignment of a preferential $\langle 001 \rangle_{\beta}$ growth direction with \vec{G}_L , which is now orientated more toward WD than ND, so that new twinned dendrite orientations will start to overgrow the original near-ND orientated grains that grew first form the base of the melt pool.

For these newly twin-reorientated dendrites to not then develop into larger columnar grains as more layers are added, their growth must also be disrupted. Along with increasing the fusion boundary inclination angle at the melt-pool rear, as the WFS is increased, the remelt depth also reduces. For standard WAAM conditions with a low WFS and a flatter melt-pool base, the remelt depth is typically ~ 60 pct^[87] of the previous layer, such that any new grains formed by twinning near the rear surface of the melt pool (which can always be seen at the top of the last pass in Figure 1) will be remelted in the next pass. These will not interrupt the normal columnar growth from the base of the melt pool where the grains are aligned closer to ND (Figure 14(a)). However, as the WFS increases, the new fusion boundary in the next layer moves up more relative to the old fusion-zone depth, and the top rear of the melt pool becomes more inclined, favoring twinning occurring to a greater depth at the melt-pool rear. When these two factors are

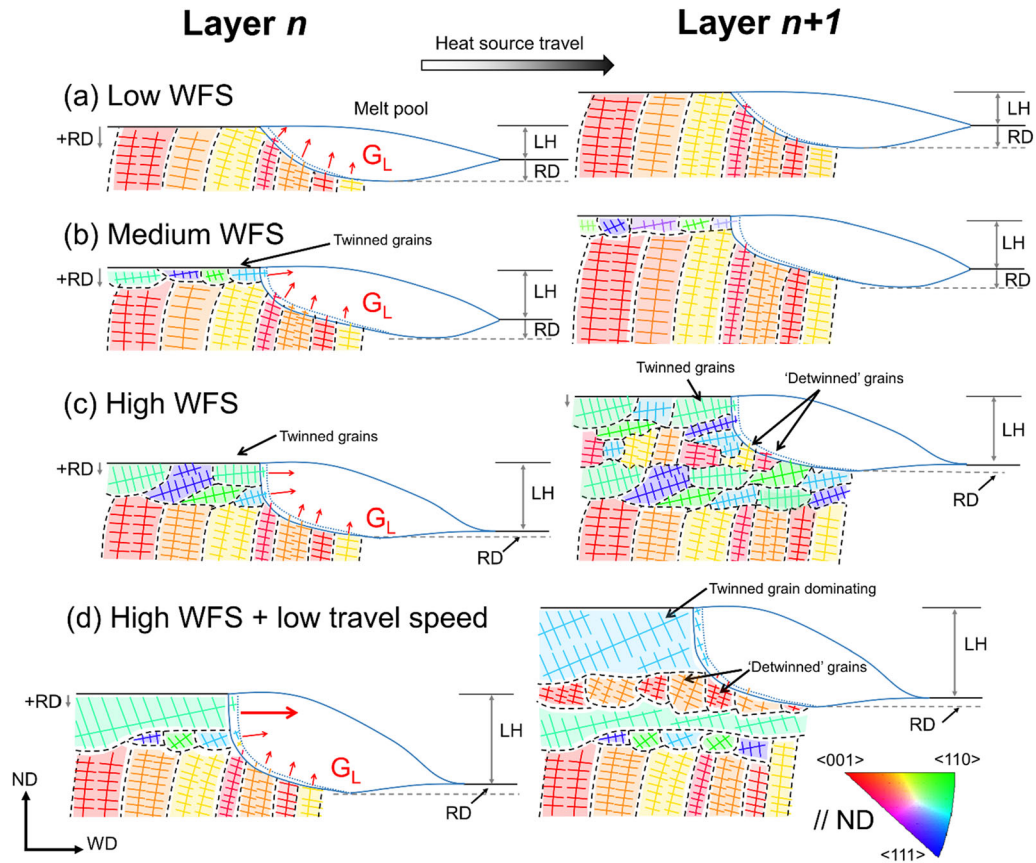


Fig. 14—Schematic diagram showing the effect of increasing wire feed speed (WFS) on the melt-pool geometry and preferential growth direction of β -phase dendrites developing at the fusion boundary in Ti alloys with a small mushy zone over two added wire layers (deposited on a columnar-grained substrate built with low WFS). The current and subsequent layer remelt depth (RD, + RD) and layer height (LH) are indicated for each scenario. β grains are colored according to the IPF ($//$ ND) system to directly match those in the EBSD maps in Fig. 1.

combined, for the optimum WFS, this has the effect that the layer of realigned twinned grains is only partially melted back during the next pass (Figures 14(a) through (c)). When not fully remelted, the twinned grains realigned toward WD then become the base of the next fusion boundary where \vec{G}_L is now close to ND, which will try to force them to grow in this direction. As they are inclined by $\sim 30\text{--}45$ deg toward WD (closest $\langle 001 \rangle_\beta$ pole to WD), this will encourage twinning back toward ND. Once realigned with ND, as solidification continues, the fusion boundary will start once again to tilt more toward WD at the top half of the melt pool, favoring twinned dendrites aligned closer to WD. Overall, this cyclic disruption to the preferred growth direction within each melt track, caused by less remelting and a more inclined melt-pool geometry that occurs with a high WFS, therefore encourages more twinning at the solidification front within each deposited layer, refining the grain structure.

Interestingly, if the WFS is too high, the results in Figures 1(d) and (e) and 4 (*i.e.*, 47 to > 50 mm/s) show that the grain size starts to increase again and more grain directionality and texture is seen in the builds. This suggests a combination of a very low remelt depth and

further tilting of the rear fusion boundary surface increases the growth distance possible before direction switching between passes, leading to more grains being able to grow further before their growth direction is disrupted; *i.e.*, the grains that nucleate aligned with the highly inclined rear of the melt pool start to form larger grains that then become elongated in between the ND and WD directions.

To better illustrate the proposed mechanism of encouraging dendrite twinning by switching the growth direction, a further more extreme sample was produced with a lower travel speed of 3 mm/s, while maintaining a high WFS at 50 mm/s. This should actually decrease the tendency for free nucleation by reducing the dendrite-tip undercooling and increasing G_L/v . However, it also has the effect of increasing the layer height and the depth of the melt pool, which better differentiates bands of grains with a tendency for alternating solidification directions. The β -grain microstructure in this sample is shown in Figure 15(a) at the wall center line in the ND-WD plane. Toward the bottom half of this map, a more regular banded grain structure can be seen which consists of two alternating bands that are produced in each deposited layer of fine $\langle 001 \rangle_\beta // \text{ND}$ (near red) orientated

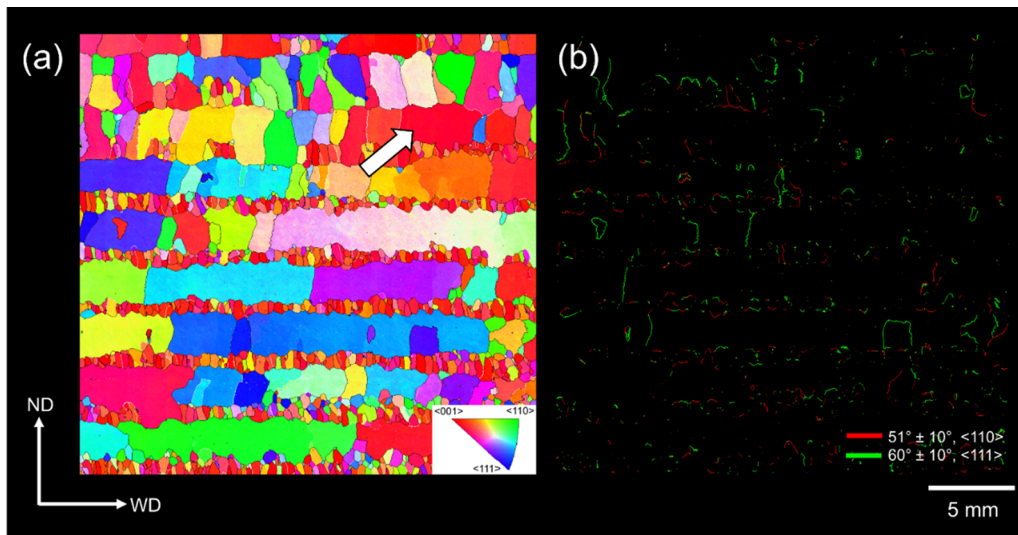


Fig. 15—Reconstructed- β EBSD map of a Ti64 sample deposited with a wire feed speed of 50 mm/s and a slower travel speed of 3 mm/s: (a) IPF orientation map and (b) the corresponding twin boundaries present.

‘columnar’ grains and larger axial grains that have grown following the heat source direction. The fine ND orientated grains have developed from the fusion boundary near the base of the melt pool when \vec{G}_L was close to ND. These bands have then been cut off by larger grains that are highly elongated in the melt-pool travel direction, WD, and are orientated more between $\langle 110 \rangle_\beta$ and $\langle 111 \rangle_\beta // ND$. In the accompanying twin boundary map in Figure 15(b), a high density of twin boundaries can be observed between the two distinctly different bands of grains. This growth selection process in response to the change in \vec{G}_L thus results in alternating layers of small $\langle 001 \rangle_\beta // ND$ grains and large, horizontal, ‘columnar,’ $\sim \langle 110 \rangle_\beta \rightarrow \langle 111 \rangle_\beta$ twinned grains (blue/green), which have reorientated their growth direction. This structure is also illustrated in the schematic diagram in Figure 14(d). However, the conditions appear to have changed slightly at the top right in Figure 15(a) (arrowed), where in some layers locally the $\langle 001 \rangle_\beta // ND$ (red) grains have survived and carried on growing up through the melt pool to become larger.

D. The Effect of Alloy Composition

The two alloys behaved similarly with increasing WFS, with respect to the grain structure transition. But, the Ti6242 alloy had a finer primary β grain structure in all the samples and underwent the grain refinement transition slightly earlier, while post-transition its grain structure was more heterogeneous and textured, although this was still weak relative to the strong texture of the conventional coarse—columnar grain structure. This more rapid transition may have been affected by small differences in melt-pool geometry between the two alloys due to, for example, the effects of their different alloying elements on the liquid surface tension and Marangoni convective flow.^[88] However,

there are significant metallurgical differences between the two alloys, caused by the greater growth restriction and slightly higher freezing range of Ti6242. In epitaxial-columnar growth, it is known that the width of the columnar grains can be substantially reduced by the addition of slower diffusing elements that partition more strongly, as has been shown in Ti64 with the addition of Y and B.^[36,37] Si in Ti6242 has a low partition coefficient ($k_{Si} = 0.33$)^[21,76] and probably behaves similarly, but less effectively than B. Mo, although segregating inversely ($k_{Mo} = 2$)^[21,22] has a very low diffusivity in Ti and helps prevent solid-state grain growth during reheating.^[77] Furthermore, the composition of Ti6242 will increase the solute undercooling and the width of the mushy zone compared to Ti64, which will lead to higher aspect ratio dendrites. Together, this may help promote twinning, and with slower growth, improve the survival rate of new twins when competing with the $\langle 001 \rangle_\beta // ND$ aligned grains, allowing the transition to occur at a lower WFS. It is also possible that the rejection of more solute in Ti6242, such as Si, increases the frequency of stacking faults that nucleate twins in this alloy. Due to stronger solutal effects, the width of the columnar grains was reduced by $\sim 3x$ in Ti6242 compared to Ti64, while the melt-pool depth and bead height were similar when depositing both alloys. The smaller width of the grains that are refined by twinning in each pass in Ti6242 thus provided more opportunity for finer grains to develop, and through growth competition, they can then obtain greater alignment with the solidification direction than in Ti64 before they are disrupted again by a change in solidification direction.

Finally, when viewed in the transverse TD-ND sections in Figure 2, it is apparent that large columnar grains can be seen at low WFS that are tilted toward the wall edges in both alloys, which follow the convex melt-pool base. In addition, in the high WFS Ti6242 alloy samples, the individual columnar grains can be seen to grow radially normal to the melt-pool curvature

(Figures 2(b) and (e)). In the low WFS Ti64 sample, grains have maintained their $\langle 001 \rangle_\beta$ alignment parallel to ND but have clearly curved sideways by adjusting the growth of their side arms (Figure 2(a)). However, there are examples of some large and more misorientated grains (with respect to ND) split in two $\langle 001 \rangle_\beta$ directions toward each wall surface; such as the yellow $\langle 012 \rangle_\beta$ //ND grain in Figure 2(a). In addition, the radial distribution of the finer columnar grains in Figure 1(e), which are ‘slab’ shaped in 3D as they are also extended in WD, cannot all be explained by twinning. This suggests that other mechanisms must be occurring in combination with twinning to realign the grains in this plane. For example, it is known that ‘stray’ grain structures can form in welding melt pools, where shorter columnar grains are observed in fusion zones that have realigned due to bending of partially remelted dendrites; or from reorientation by dendrite fragments that melt off at the solidification front.^[25,89] In Ti6242, the slightly larger freezing range and wider mushy zone may help promote nucleation of additional grains by dendrite fragmentation, which can also occur at very low undercoolings.^[25,89] Lattice rotation caused by dislocations can also allow dendrites to bend and follow a curving growth front,^[25] but unfortunately this cannot be reliably detected with the current β -reconstruction technique. A further possibility is the appearance of new β -grain orientations induced by the $\alpha \rightarrow \beta$ phase transformation during WAAM cyclical reheating,^[90] which is capable of producing the grain orientation relationships seen in this work (*e.g.*, Figure 10). However, in Ti64 this has only been seen when significant plastic strain is applied to each layer by inter-pass deformation techniques like rolling or peening.^[30,33] Since increasing the WFS affects only the initial solidification and not the subsequent reheating, this mechanism would not be expected to be affected by increasing the WFS, unless this has a dramatic effect on the residual stress development (*e.g.*, Figure 1(a)). So, although the curved solidification front-induced twinning appears to be prevalent in the EBSD measurements of the grain structures, and is largely responsible for the transition in grain structure with WFS, other mechanisms of dendrite reorientation and β -grain nucleation are also important. It is also apparent that changing the travel direction for each pass with conditions that give an optimally inclined melt-pool surface would be more effective in refining the grain structure and this would explain why reversing the travel direction has been claimed to be beneficial in some AM processes.^[91]

V. CONCLUSIONS

It is technologically important to improve the coarse and directional primary (BCC) β -grain structures in Ti alloys currently produced by high deposition rate AM processes, because of their detrimental effect on mechanical performance. By increasing the wire feed speed, a dramatic transition from a strongly textured coarse and columnar grain structure to a weakly textured, fine, and

near-equiaxed structure has been observed in two $\alpha + \beta$ Ti alloys; Ti64 and Ti6242. By applying the KGT tip undercooling model, calculating Hunt CET solidification maps, and using a CFD model to estimate the solidification conditions, it has been shown that without the presence of efficient nucleants, this is unlikely to have occurred by free nucleation in an undercooled liquid ahead of the columnar growth front. Instead, experimental evidence of copious dendrite twinning was found within the refined grain structures.

Estimates of the dendrite-tip undercooling in Ti64 suggest that, due to very low solute partitioning in Ti64, it is too small (< 2 K) for free nucleation in the melt pool and it is also difficult to increase sufficiently to promote a CET within the process stability constraints of a standard plasma transferred arc WAAM process, unless inoculation is introduced. CFD melt-pool simulations also showed that the key solidification parameters, G_L and v , did not change greatly with WFS and remained within the columnar region on the Kobryn-Semiatin Hunt map.^[26,46]

At low wire feed speeds, twin relationships were found between small skin grains and island grains embedded within the coarse and columnar grains in the samples’ centers. A high fraction of 60 deg- $\langle 111 \rangle_\beta$ and a lower density of 51 deg- $\langle 110 \rangle_\beta$ boundaries were also seen in EBSD maps of the refined β -grain structures at high wire feed speeds, which are consistent with $\{112\}_\beta \langle 111 \rangle_\beta$ and $\{332\}_\beta \langle 113 \rangle_\beta$ BCC twinning systems, respectively.

It is shown that departure from $\langle 001 \rangle_\beta$ alignment with the direction of maximum thermal gradient in the liquid, \vec{G}_L , due to curvature of the melt-pool fusion boundary promoted twinning in both alloys. Increasing the wire feed speed led to a larger bead height and lower remelt depth, which tilted the melt pool toward the travel direction, increasing the inclination angle at the rear of the fusion boundary. This change in melt-pool geometry, and the reduction in remelt depth with wire feed speed, led to increasing disruption to the solidification direction within each layer, promoting twinning and grain refinement.

Finally, exploiting this mechanism for refining the β grains in Ti WAAM by promoting disruption to the crystal growth directions by controlling the melt-pool geometry and remelt depth would be more convenient than applying other processes such as inter-pass deformation,^[33] or ultrasonic vibration.^[38] However, such an approach is not without its restrictions, as the conditions that facilitate β -grain refinement are limited by process stability and lead to less part accuracy; *i.e.*, a high bead height with a low remelt depth will increase wall edge roughness.

ACKNOWLEDGMENTS

The authors are appreciative of the EPSRC program grants NEWAM (EP/R027218/1) and Light-Form (EP/R001715/1), for supporting aspects of this research. The authors acknowledge the use of

equipment associated with the Advanced Metals Processing and Characterization themes of the Henry Royce Institute for Advanced Materials, funded through EPSRC grants EP/R00661X/1, EP/S019367/1, EP/P025021/1, and EP/P025498/1. P.B. Prangnell is grateful to the Royal Academy of Engineering, UK, and Airbus for supporting his research through the Airbus-University of Manchester Centre for Metallurgical Excellence.

CONFLICT OF INTEREST

On behalf of all the authors, the corresponding author states that there is no conflict of interest.

OPEN ACCESS

This article is licensed under a Creative Commons Attribution 4.0 International License, which permits use, sharing, adaptation, distribution and reproduction in any medium or format, as long as you give appropriate credit to the original author(s) and the source, provide a link to the Creative Commons licence, and indicate if changes were made. The images or other third party material in this article are included in the article's Creative Commons licence, unless indicated otherwise in a credit line to the material. If material is not included in the article's Creative Commons licence and your intended use is not permitted by statutory regulation or exceeds the permitted use, you will need to obtain permission directly from the copyright holder. To view a copy of this licence, visit <http://creativecommons.org/licenses/by/4.0/>.

REFERENCES

1. S.W. Williams, F. Martina, A.C. Addison, J. Ding, G. Pardal, and P.A. Colegrove: *Mater. Sci. Technol.*, 2016, vol. 32(7), pp. 641–47. <https://doi.org/10.1179/1743284715Y.0000000073>.
2. D. Ding, Z. Pan, D. Cuiuri, and H. Li: *Int. J. Adv. Manuf. Technol.*, 2015, vol. 81(1–4), pp. 465–81. <https://doi.org/10.1007/s00170-015-7077-3>.
3. X. Bai, et al.: *Int. J. Heat Mass Transf.*, 2018, vol. 124, pp. 504–16. <https://doi.org/10.1016/j.ijheatmasstransfer.2018.03.085>.
4. A. Ho, H. Zhao, J.W. Fellowes, F. Martina, A.E. Davis, and P.B. Prangnell: *Acta Mater.*, 2019, vol. 166, pp. 306–23. <https://doi.org/10.1016/j.actamat.2018.12.038>.
5. H. Zhao, A. Ho, A.E. Davis, A.A. Antonysamy, and P.B. Prangnell: *Mater. Charact.*, 2019, vol. 147, pp. 131–45. <https://doi.org/10.1016/j.matchar.2018.10.027>.
6. A. Caballero, et al.: *Philos. Mag.*, 2022, vol. 102(22), pp. 2256–81. <https://doi.org/10.1080/14786435.2022.2113470>.
7. J. Wang, et al.: *J. Alloys Compd.*, 2018, vol. 768, pp. 97–113. <https://doi.org/10.1016/j.jallcom.2018.07.235>.
8. F. Martina, S.W. Williams, and P.A. Colegrove: Improved microstructure and increased mechanical properties of additive manufacture produced Ti-6Al-4V by interpass cold rolling. in *SFF Symp.*, pp. 490–96, 2013, <https://doi.org/10.1007/s13398-014-0173-7.2>.
9. M.J. Bermingham, D.H. StJohn, J. Krynen, S. Tedman-Jones, and M.S. Dargusch: *Acta Mater.*, 2019, vol. 168, pp. 261–74. <https://doi.org/10.1016/j.actamat.2019.02.020>.
10. F. Wang, S.W. Williams, P.A. Colegrove, and A.A. Antonysamy: *Metall. Mater. Trans. Phys. Metall. Mater. Sci.*, 2013, vol. 44(2), pp. 968–77. <https://doi.org/10.1007/s11661-012-1444-6>.
11. L. Neto, S.W. Williams, J. Ding, J.R. Hönnige, and F. Martina: Mechanical Properties Enhancement of Additive Manufactured Ti-6Al-4V by Machine Hammer Peening. in *Adv. Surf. Enhanc. 1st Int. Conf. Adv. Surf. Enhanc.*, vol. 1, pp. 121–32, 2020. <https://doi.org/10.1007/978-981-15-0054-1>.
12. A.K. Syed, et al.: *Mater. Sci. Eng. A*, 2021, vol. 814, p. 141194. <https://doi.org/10.1016/j.msea.2021.141194>.
13. X. Zhang, F. Martina, J. Ding, X. Wang, and S.W. Williams: *Fatigue Fract. Eng. Mater. Struct.*, 2017, vol. 40(5), pp. 790–803. <https://doi.org/10.1111/ffe.12547>.
14. E. Brandl, B. Baufeld, C. Leyens, and R. Gault: *Phys. Procedia*, 2010, vol. 5(2), pp. 595–606. <https://doi.org/10.1016/j.phpro.2010.08.087>.
15. S.M. Kelly and S.L. Kampe: *Metall. Mater. Trans. A*, 2004, vol. 35A, pp. 1861–67. <https://doi.org/10.1007/s11661-004-0095-7>.
16. S.M. Kelly and S.L. Kampe: *Metall. Mater. Trans. A*, 2004, vol. 35A, pp. 1869–79.
17. J.W. Elmer, T.A. Palmer, and J. Wong: *J. Appl. Phys.*, 2003, vol. 93(4), pp. 1941–47. <https://doi.org/10.1063/1.1537464>.
18. S. Malinov, P. Markovsky, W. Sha, and Z. Guo: *J. Alloys Compd.*, 2001, vol. 314, pp. 181–92. [https://doi.org/10.1016/S0925-8388\(00\)01227-5](https://doi.org/10.1016/S0925-8388(00)01227-5).
19. G. Lütjering and J.C. Williams: *Titanium*, Springer, New York, 2007.
20. D. Lunt, et al.: *Mater. Sci. Eng. A*, 2020, vol. 788, p.139608. <https://doi.org/10.1016/j.msea.2020.139608>.
21. M.J. Bermingham, S.D. McDonald, M.S. Dargusch, and D.H. StJohn: *J. Mater. Res.*, 2008, vol. 23(1), pp. 97–104. <https://doi.org/10.1557/jmr.2008.0002>.
22. T. Lyman: *Atlas of Microstructures of Industrial Alloys*. American Society for Metals, 1972.
23. D.A. Porter and K.E. Easterling: *Phase Transformations in Metals and Alloys*, vol. 3. 1992. <https://doi.org/10.1146/annurev.ms.03.080173.001551>.
24. S.A. David and J.M. Vitek: *Int. Mater. Rev.*, 1989, vol. 34(1), pp. 213–45. <https://doi.org/10.1179/imr.1989.34.1.213>.
25. S.A. David, S.S. Babu, and J.M. Vitek: *JOM*, 2003, vol. 55(6), pp. 14–20. <https://doi.org/10.1007/s11837-003-0134-7>.
26. J.D. Hunt: *Mater. Sci. Eng.*, 1984, vol. 65(1), pp. 75–83. [https://doi.org/10.1016/0025-5416\(84\)90201-5](https://doi.org/10.1016/0025-5416(84)90201-5).
27. W. Kurz, C. Bezençon, and M. Gäumann: *Sci. Technol. Adv. Mater.*, 2001, vol. 2(1), pp. 185–91. [https://doi.org/10.1016/S1468-6996\(01\)00047-X](https://doi.org/10.1016/S1468-6996(01)00047-X).
28. H. Nguyen-Thi, et al.: *Metall. Mater. Trans. A*, 2007, vol. 38A, pp. 1458–64. <https://doi.org/10.1007/s11661-007-9170-1>.
29. J.R. Kennedy, et al.: *Mater. Charact.*, 2021, vol. 182, p. 111577. <https://doi.org/10.1016/j.matchar.2021.111577>.
30. J.R. Hönnige, et al.: *Metall. Mater. Trans. A*, 2020, vol. 51A, pp. 3692–3703.
31. S.L. Semiatin, J.C. Soper, and I.M. Sukonnik: *Acta Metall.*, 1996, vol. 44(5), pp. 1979–86. [https://doi.org/10.1016/1359-6454\(95\)00311-8](https://doi.org/10.1016/1359-6454(95)00311-8).
32. A.E. Davis, J.R. Kennedy, J. Ding, and P.B. Prangnell: *Mater. Charact.*, 2020, vol. 163, p. 110298. <https://doi.org/10.1016/j.matchar.2020.110298>.
33. J. Donoghue, A.A. Antonysamy, F. Martina, P.A. Colegrove, S.W. Williams, and P.B. Prangnell: *Mater. Charact.*, 2016, vol. 114, pp. 103–14. <https://doi.org/10.1016/j.matchar.2016.02.001>.
34. J.R. Kennedy, et al.: *Mater. Lett. X*, 2020, vol. 8, p. 100057. <https://doi.org/10.1016/j.mlblux.2020.100057>.
35. J.R. Kennedy, A.E. Davis, A. Caballero, S.W. Williams, E.J. Pickering, and P.B. Prangnell: *Addit. Manuf.*, 2021, vol. 40, p. 101928. <https://doi.org/10.1016/j.addma.2021.101928>.
36. J.R. Kennedy, et al.: *J. Alloys Compd.*, 2022, vol. 895, p. 162735. <https://doi.org/10.1016/j.jallcom.2021.162735>.
37. K. Zhang, et al.: *Mater. Des.*, 2019, vol. 184, p. 108191. <https://doi.org/10.1016/j.matdes.2019.108191>.
38. C.J. Todaro, et al.: *Nat. Commun.*, 2020, vol. 11(1), p. 142. <https://doi.org/10.1038/s41467-019-13874-z>.
39. F. Wang, S.W. Williams, and M. Rush: *Int. J. Adv. Manuf. Technol.*, 2011, vol. 57(5–8), pp. 597–603. <https://doi.org/10.1007/s00170-011-3299-1>.
40. E. Farabi, T. Klein, M. Schnell, and S. Primig: *Addit. Manuf.*, 2023, <https://doi.org/10.1016/j.addma.2023.103592>.
41. A.I. Saville, et al.: *Addit. Manuf.*, 2021, vol. 46, p. 102118. <https://doi.org/10.1016/j.addma.2021.102118>.

42. A.E. Davis, J.R. Kennedy, D. Strong, D. Kovalchuk, S. Porter, and P.B. Prangnell: *Materialia*, 2021, vol. 20, p. 101202. <https://doi.org/10.1016/j.mta.2021.101202>.
43. C. Jing, et al.: *Mater. Sci. Eng. A*, 2022, vol. 845, p. 143223. <https://doi.org/10.1016/j.msea.2022.143223>.
44. B. Wu, et al.: *Addit. Manuf.*, 2022, vol. 54, p. 102723. <https://doi.org/10.1016/j.addma.2022.102723>.
45. J. Wang, et al.: *Mater. Sci. Eng. A*, 2020, vol. 772, p. 138703. <https://doi.org/10.1016/j.msea.2019.138703>.
46. P.A. Kobryn and S.L. Semiatin: *J. Mater. Process. Technol.*, 2003, vol. 135(2–3), pp. 330–39. [https://doi.org/10.1016/S0924-0136\(02\)00865-8](https://doi.org/10.1016/S0924-0136(02)00865-8).
47. W. Kurz, B. Giovanola, and R. Trivedi. *Acta Metall.*, 1985.
48. J. Wainwright: *Grain Structure Control of Titanium Alloys During Wire + Arc Additive Manufacturing*, Cranfield University, Bedford, 2023.
49. J. Wainwright, S. Williams, and J. Ding: *Addit. Manuf.*, 2023, vol. 74, p. 103712. <https://doi.org/10.1016/j.addma.2023.103712>.
50. P.S. Davies: *An Investigation of Microstructure and Texture Evolution in the Near- α Titanium Alloy Timetal 834*, University of Sheffield, Sheffield, 2009.
51. P.S. Davies, B.P. Wynne, W.M. Rainforth, M.J. Thomas, and P.L. Threadgill: *Metall. Mater. Trans. Phys. Metall. Mater. Sci.*, 2011, vol. 42(8), pp. 2278–89. <https://doi.org/10.1007/s11661-011-0606-2>.
52. G. Ivantsov: *Dokl. Akad. Nauk SSSR*, 1947, vol. 58, pp. 567–69.
53. J. Strickland, B. Nenechev, and H. Dong: *Crystals*, 2020, vol. 10(7), p. 627. <https://doi.org/10.3390/cryst10070627>.
54. W.W. Mullins and R.F. Sekerka: Stability of a Planar Interface During Solidification of a Dilute Binary Alloy, in *Dynamics of Curved Fronts*, Elsevier, 1988, pp. 345–52. <https://doi.org/10.1016/B978-0-08-092523-3.50037-X>.
55. W. Kurz and D.J. Fisher: *Acta Metall.*, 1981, vol. 29(1), pp. 11–20. [https://doi.org/10.1016/0001-6160\(81\)90082-1](https://doi.org/10.1016/0001-6160(81)90082-1).
56. J.S. Langer and H. Muller-Krumbhaar: Stability Effects in Dendritic Crystal Growth *t*.
57. C.-A. Gandin and M. Rappaz: *Acta Mater.*, 1997, vol. 45(5), pp. 2187–95. [https://doi.org/10.1016/S1359-6454\(96\)00303-5](https://doi.org/10.1016/S1359-6454(96)00303-5).
58. J.-O. Andersson, T. Helander, L. Höglund, P. Shi, and B. Sundman: *Calphad*, 2002, vol. 26(2), pp. 273–312. [https://doi.org/10.1016/S0364-5916\(02\)00037-8](https://doi.org/10.1016/S0364-5916(02)00037-8).
59. D.M. Stefanescu: Equilibrium and non-equilibrium during solidification, in *Science and Engineering of Casting Solidification, Second Edition*. Boston: Springer, 2009, pp. 1–20. https://doi.org/10.1007/978-0-387-74612-8_2.
60. D. Dreelan: Meso-scale Grain Structure Prediction Models for Metallic Additive Manufacturing Processes, PhD Thesis, University College Dublin, 2022.
61. L. Wu and J. Zhang: *JOM*, 2018, vol. 70(10), pp. 2392–99. <https://doi.org/10.1007/s11837-018-3057-z>.
62. R.E. Rozas, L.G. MacDowell, P.G. Toledo, and J. Horbach: *J. Chem. Phys.*, 2021, vol. 154(18), p. 184704. <https://doi.org/10.1063/5.0049131>.
63. L. Ding, et al.: *Metals*, 2020, vol. 10(8), p. 989. <https://doi.org/10.3390/met10080989>.
64. J. Song, L. Wang, L. Zhang, W. Wu, and Z. Gao: *J. Mol. Liq.*, 2020, vol. 315, p. 113606. <https://doi.org/10.1016/j.molliq.2020.113606>.
65. X. Chen, C. Wang, J. Ding, P. Bridgeman, and S. Williams: *J. Manuf. Process.*, 2022, vol. 83, pp. 300–12. <https://doi.org/10.1016/j.jmapro.2022.09.012>.
66. C.W. Hirt and B.D. Nichols: *J. Comput. Phys.*, 1981, vol. 39(1), pp. 201–25. [https://doi.org/10.1016/0021-9991\(81\)90145-5](https://doi.org/10.1016/0021-9991(81)90145-5).
67. V.R. Voller, A.D. Brent, and C. Prakash: *Int. J. Heat Mass Transf.*, 1989, vol. 32(9), pp. 1719–31. [https://doi.org/10.1016/0017-9310\(89\)90054-9](https://doi.org/10.1016/0017-9310(89)90054-9).
68. R. Hu, X. Chen, G. Yang, S. Gong, and S. Pang: *Int. J. Heat Mass Transf.*, 2018, vol. 126, pp. 877–87. <https://doi.org/10.1016/j.ijheatmasstransfer.2018.06.033>.
69. B.A. Welk, N. Taylor, Z. Kloenne, K.J. Chaput, S. Fox, and H.L. Fraser: *Metall. Mater. Trans. Phys. Metall. Mater. Sci.*, 2021, vol. 52(12), pp. 5367–80. <https://doi.org/10.1007/s11661-021-06475-3>.
70. R.P. Mooney, et al.: *Comput. Mater. Sci.*, 2022, vol. 210, p. 111436. <https://doi.org/10.1016/j.commatsci.2022.111436>.
71. P. Schempp, Z. Tang, C. Cross, T. Seefeld, A. Pittner, and M. Rethmeier: *Trends Weld. Res.* 2012.
72. R.C. Atwood, P.D. Lee, R.S. Minisandram, and R.M.F. Jones: *J. Mater. Sci.*, 2004, vol. 39(24), pp. 7193–97. <https://doi.org/10.1023/B:JMSS.0000048731.42495.1c>.
73. Q. Liu, X. Li, and Y. Jiang: *Vacuum*, 2017, vol. 141, pp. 1–9. <https://doi.org/10.1016/j.vacuum.2017.03.009>.
74. Q.-L. Liu, X.-M. Li, and Y.-H. Jiang: *J. Mater. Res.*, 2017, vol. 32(16), pp. 3175–82. <https://doi.org/10.1557/jmr.2017.174>.
75. J.K. Mackenzie: Second Paper on Statistics Associated with the Random Disorientation of Cubes.
76. A.A. Nayeb-Hashemi and J.B. Clark: *Phase Diagrams of Binary Magnesium Alloys*, ASM International, Detroit, 1988.
77. A.E. Davis, A.E. Caballero, R. Biswal, S.W. Williams, and P.B. Prangnell: *Metall. Mater. Trans. A*, 2022, vol. 53A, pp. 3833–52. <https://doi.org/10.1007/s11661-022-06811-1>.
78. E. Bertrand, P. Castany, I. Péron, and T. Gloriant: *Scr. Mater.*, 2011, vol. 64(12), pp. 1110–13. <https://doi.org/10.1016/j.scriptamat.2011.02.033>.
79. S. Hanada and O. Izumi: *Metall. Trans. A*, 1986, vol. 17, pp. 1409–20.
80. A. Greer, A. Bunn, A. Tronche, P. Evans, and D. Bristow: *Acta Mater.*, 2000, vol. 48, pp. 2823–35.
81. J.L. McClure and A. Cezairliyan: *Int. J. Thermophys.*, 1992, vol. 13(1), pp. 75–81. <https://doi.org/10.1007/BF00503357>.
82. D. Bandyopadhyay, R.C. Sharma, and N. Chakraborti: *J. Phase Equilibria*, 2000, vol. 21(2), pp. 179–85. <https://doi.org/10.1361/105497100770340246>.
83. M.A. Salgado-Ordorica and M. Rappaz: *Acta Mater.*, 2008, vol. 56(19), pp. 5708–18. <https://doi.org/10.1016/j.actamat.2008.07.046>.
84. M.A. Salgado-Ordorica, J.-L. Desbiolles, and M. Rappaz: *Acta Mater.*, 2011, vol. 59(13), pp. 5074–84. <https://doi.org/10.1016/j.actamat.2011.04.033>.
85. J.J. Hoyt and M. Asta: *Phys. Rev. B*, 2002, vol. 65(21), p. 214106. <https://doi.org/10.1103/PhysRevB.65.214106>.
86. Ø. Grong and I. of M. (Great Britain), *Metallurgical Modelling of Welding*. in Book (Institute of Materials (Great Britain)). Institute of Materials, 1997. <https://books.google.co.uk/books?id=JwNUAAAAMAAJ>.
87. A. Caballero: Dilution study Ti-6Al-4V LAMP project, 2018.
88. K. Weman: *Welding Processes Handbook*, Woodhead Publishing Limited, Cambridge, 2012.
89. N. Ren, J. Li, N. Bogdan, M. Xia, and J. Li: *Comput. Mater. Sci.*, 2020, vol. 180, p. 109714. <https://doi.org/10.1016/j.commatsci.2020.109714>.
90. C. Cayron: *Scr. Mater.*, 2008, vol. 59(5), pp. 570–73. <https://doi.org/10.1016/j.scriptamat.2008.05.013>.
91. A.A. Antonyamy, J. Meyer, and P.B. Prangnell: *Mater Charact.*, 2013, vol. 84, pp. 153–68. <https://doi.org/10.1016/j.matchar.2013.07.012>.

Publisher's Note Springer Nature remains neutral with regard to jurisdictional claims in published maps and institutional affiliations.